Simulated response of South Atlantic Subtropical Mode Water to air-sea processes

Piero Silveira Bernardo[1], Olga T. Sato[2], and Andrea Sardinha Taschetto[3]

[1]University of São Paulo
[2]University of Sao Paulo
[3]University of New South Wales

November 22, 2022

Abstract

Subtropical mode water is formed in winter-time deep mixed layer due to variations in air-sea processes. In the South Atlantic, three formation cores are identified between 30oS and 40oS: in the west, in the east, and north of the Subtropical Front. Each one of these three types presents typical mean thickness and horizontal distribution patterns, mainly because of local dynamic and thermodynamic characteristics of each part of the basin. In this study we assess the effects of momentum, freshwater and radiative fluxes on the variation in volume and composition of the South Atlantic Subtropical Mode Water (SASTMW). Sensitivity experiments were designed using the National Center for Atmospheric Research Community Earth System Model. Multiple one-year simulations are forced with varying intensity of wind, precipitation and shortwave radiation. By comparing to a control run, we were able to determine that the water volume variations in the east (SASTMW type 1) and south (SASTMW type 3) are significantly affected by precipitation and shortwave radiation, and thus are more sensitive to thermodynamic processes. On the other hand, SASTMW type 2 has a greater relationship with dynamic processes and is influenced by the Indian–Atlantic interbasin exchanges.

Simulated response of South Atlantic Subtropical Mode Water to air-sea processes

Piero S. Bernardo[1], Olga T. Sato[1] and Andréa S. Taschetto[2]

[1]Oceanographic Institute of the University of São Paulo, São Paulo, Brazil
[2]Climate Change Research Centre and ARC Centre of Excellence for Climate Extremes, University of New South Wales, Sydney, Australia

Key Points:

- In the South Atlantic the subtropical mode waters are linked to different forcings.
- SASTMW1 and SASTMW3 are related primarily to thermodynamic processes.
- SASTMW2 is affected mainly by dynamical processes and is influenced by inter-basin exchanges linked to the Agulhas Leakage.

Corresponding author: Piero S. Bernardo, `piero.bernardo@usp.br`

Abstract

Subtropical mode water is formed in winter-time deep mixed layer due to variations in air-sea processes. In the South Atlantic, three formation cores are identified between 30°S and 40°S: in the west, in the east, and north of the Subtropical Front. Each one of these three types presents typical mean thickness and horizontal distribution patterns, mainly because of local dynamic and thermodynamic characteristics of each part of the basin. In this study we assess the effects of momentum, freshwater and radiative fluxes on the variation in volume and composition of the South Atlantic Subtropical Mode Water (SASTMW). Sensitivity experiments were designed using the National Center for Atmospheric Research Community Earth System Model. Multiple one-year simulations are forced with varying intensity of wind, precipitation and shortwave radiation. By comparing to a control run, we were able to determine that the water volume variations in the east (SASTMW type 1) and south (SASTMW type 3) are significantly affected by precipitation and shortwave radiation, and thus are more sensitive to thermodynamic processes. On the other hand, SASTMW type 2 has a greater relationship with dynamic processes and is influenced by the Indian–Atlantic interbasin exchanges.

1 Introduction

The formation of mode water in the subtropics is highly related to the development of a deep winter mixed layer (Oka & Qiu, 2012). It is characterized as a quasi-homogeneous vertical layer with low potential vorticity (PV) values (Hanawa & Talley, 2001). After its formation cycle, a pycnostad layer is trapped between the seasonal and main thermocline, and it can be advected away from the formation site (Joyce et al., 2013).

Warren (1972) and Worthington (1976) have shown that the formation of the North Atlantic Subtropical Mode Water, also known as the Eighteen Degree Water, is related to both thermodynamic and dynamic processes. The main portion is formed due to an intense cooling process of the surface during the winter months (Hanawa & Talley, 2001). During that period, the ocean loses heat through its interface for the atmosphere, which reduces the sea surface temperature. That causes an increase in the density of the upper layers and thus reduces its buoyancy. The portion of the ocean affected by heat loss is led to a convective process, generating low density gradients and, consequently, low PV values. Deeper mixing layers are then formed (Worthington, 1972), which can potentially transform into mode water layers (McCartney & Talley, 1982).

The volume formed due to the buoyancy flux within a determined range of density can be estimated through the methodology developed by Walin (1982). The formation related to dynamic processes, on the other hand, can be attributed to processes at the ocean–atmosphere interface, such as wind, Ekman transport and eddies (Qiu et al., 2007; J. W. Holte et al., 2012). These phenomena can intensify the process of deep convection causing thickening of the water columns.

The formation of mode waters can be identified in the polar and subtropical regions (Hanawa & Talley, 2001). When contained within a subtropical gyre, it is called subtropical mode water (STMW) (Masuzawa, 1969). It is possible to observe it in all ocean basins, linked to regions of permanent fronts (Hanawa & Talley, 2001) as the well-known Eighteen Degree Water (Worthington, 1959) and the North Pacific STMW (Masuzawa, 1969). In general, the existence of up to four types of STMW can be related to their place of formation, density, salinity, and/or typical stratification (Talley, 1999; Hanawa & Talley, 2001), namely: *Type I* is related to western boundary current extensions; *Type II* is associated with the eastern portion of the subtropical gyres, low density and higher stratification (Roemmich & Cornuelle, 1992); *Type III* is related to subpolar fronts, has the highest density compared to other types; and, *Type IV* can be considered as the Subtropical Underwater (Worthington, 1976) and is related to shallow salinity extrema.

To understand the formation of SASTMW we must take into account both the local dynamic and thermodynamic characteristics of the South Atlantic (Bernardo & Sato, 2020). The South Atlantic subtropical gyre is formed by four main currents: the western boundary current, Brazil Current (BC) (Stramma, 1989), which flows south along the Brazilian coast; the South Atlantic Current (Stramma & Peterson, 1990), that crosses the basin from east to west on the south side of the gyre; the Benguela Current (Stramma & Peterson, 1989) that flows northward on the eastern edge; and, the east-to-west South Equatorial Current that closes the gyre in the north part of the basin (Peterson & Stramma, 1991; Silveira et al., 1994). Within this configuration, only the southern portion of the basin is related to the South Atlantic STMW (SASTMW).

The first observations of the SASTMW were conducted by Tsuchiya et al. (1994). Later, Provost et al. (1999) observed three STMW types in the South Atlantic, related to three main ventilation windows: in the southern part of the recirculation region of the BC (western portion), related to the Brazil-Malvinas Confluence (BMC); in the east, linked to the Agulhas Leakage and Retroflection; and in the southern branch of the subtropical gyre, close to the Subtropical Front (STF). Thus, mode water formation in the South Atlantic preferably occurs between 30°S and 40°S (Bernardo & Sato, 2020), during the austral winter and in the region where there is a negative cumulative heat flux (Sato & Polito, 2014).

Due to the thermohaline contrast identified between BC and Malvinas Current (colder than the BC (Gordon & Greengrove, 1986)), the BMC is considered a region of intense dynamics and instability (Escoffier & Provost, 1998), presenting an intense thermal front with horizontal gradients around 1°C/250 m (Garzoli & Garraffo, 1989), which alter the region's vertical thermal structure (Garzoli & Bianchi, 1987). Thus, it is considered one of the most energetic regions among the oceans (Pezzi et al., 2005). Consequently, we can identify intense gradients of energy and momentum flux, which vertically influence the atmosphere and oceanic thermodynamics, generating deep convective processes leading to vigorous mixing (Ferreira et al., 2019). For these reasons, BMC can be considered an important source of thermostats (Gordon, 1981).

Along with the BMC we can observe the STF of the South Atlantic (Legeckis & Gordon, 1982) that extends eastward to the Indian Ocean and forms due to the strong meridional temperature gradients during spring and summer time (Deacon & Britain, 1937). Related to this feature, another mode water formation can also be considered important for the composition of SASTMW and the Central Waters in the South Atlantic. This one is the Subantarctic Mode Water, which is formed between the Subantarctic Front and the STF (McCartney, 1977). McCartney and Talley (1982) reported exchanges between subantarctic and subtropical waters through the use of the PV as a tracer.

The last important feature for the SATMW formation is the Agulhas Current (Gordon, 1985), more specifically the leakage of the eddies from the Indian Ocean (Duncombe Rae, 1991). According to Olson et al. (1992), the Agulhas Retroflection introduces relatively warmer and more saline waters in the South Atlantic and that amount transported is associated with westerly winds (Biastoch et al., 2009; Beal et al., 2011). The subpolar air masses trigger the sinking of these Indian Ocean waters in the South Atlantic. Thus, there is a consequent influence on the formation of SASTMW (Gordon, 1985; Fine et al., 1988).

General circulation models have been a useful tool to simulate subtropical mode waters (Hosoda et al., 2001; Rainville et al., 2007; Xu et al., 2012; Maze et al., 2013; Dong & Kelly, 2013) and to understand their different formation processes (Douglass et al., 2013) and associated variability (Peng et al., 2006; Douglass et al., 2012; Li, 2012). While most of the studies focus on the North Atlantic, North and South Pacific, there are no studies to our knowledge that have used ocean circulation models to investigate subtropical mode water in the South Atlantic Ocean. We are particularly interested in understanding the contribution of the atmospheric factors that lead to the formation of SASTMW.

Previous studies have shown that the most relevant atmospheric processes linked to the formation of mode waters (subtropical and subpolar) are the heat, freshwater and momentum fluxes (Hazeleger & Drijfhout, 1998; Rintoul & England, 2002; Kouketsu et al., 2011; J. W. Holte et al., 2012; Kelly & Dong, 2013). Changes in the air-sea interaction during winter can impact the variations in physical and spatial characteristics of mode waters (Hanawa & Talley, 2001) beyond seasonal timescales. Studies have shown decadal variability of mode water formation in other basins (Qiu & Chen, 2006), with important implications for long term heat storage capacity. Thus, a better understanding of the atmospheric and oceanic processes and what conditions are involved in the formation of mode water will contribute to studies on long-term changes at mid-latitude oceans.

In this study, we use several atmospheric scenarios through model simulation to understand the processes behind mode water formation in the South Atlantic. In a succinct way, sensitivity tests were performed to examine the response of the SASTMW types to the changes in the solar shortwave radiation, precipitation and wind.

2 Data and Methods

The study relies on four different data sets that were used in two stages. For the first part, we sought to understand what kind of relationship is there between the formation and some atmospheric variables using reanalyses. In the second part, we explored the processes that led to mode water formation using sensitive numerical experiments.

The first step of the evaluation was the identification of SASTMW. We use monthly mean temperature and salinity profiles from In Situ Analysis System (ISAS-15) and the ISAS-NRT (Near Real Time) (Gaillard et al., 2016; Kolodziejczyk et al., 2017) between 2002 to 2019. ISAS-15 encompasses the period 2002 to 2014 while ISAS-NRT covers the remaining period from 2015 to 2019. Both data sets are gridded products based on Argo observations and they were treated as one, and hereafter referred to as ISAS. After that, we use correlation analysis to assess the statistical relationship between the SASTMW formation and the net heat flux (using the turbulent and radiative fluxes), precipitation minus evaporation, and 10-meter wind speed. For the correlations with atmospheric variables we used the monthly ERA5 data set from the European Centre for Medium-Range Weather Forecasts (ECMWF) (Hersbach et al., 2019), for the same period (2002 to 2019).

Due to the absence of data with high temporal resolution covering the extension of the South Atlantic we resorted to the use of numerical simulations to observe an average annual cycle of formation in the surface and establishment of SASTMW in the subsurface. The second part of the analysis is based on numerical simulations performed with the Community Earth System Model v.1.2.2 (CESM1.2.2, hereafter referred to as CESM) (Kay et al., 2015) from the National Center for Atmospheric Research (NCAR). The CESM is a fully-coupled, global climate mode that allows different scenarios and configurations to simulate simultaneously several terrestrial systems, using up to seven geophysical models in varied periods of time (Hurrell et al., 2013) (more details in Text S1). We use the model to evaluate the formation of SASTMW in daily resolution in a control run and in the developed experiments.

2.1 Model description and experimental design

The configuration of the fully coupled CESM model was based on the need to understand how the ocean responds to an average atmospheric year (from 1948 to 2009) and the consequent mode water formation, without the obligation to observe the ocean's feedback to the atmosphere. Therefore, it was necessary for the ocean (POP) and sea–ice (CSIM) to be an active component in the model and the land (CLM) and atmospheric (CAM5) contribution to be a data component, i.e. the atmosphere forces the ocean but does not respond to ocean fields.

The model was forced with the Coordinated Ocean-Ice Reference Experiments Version 2 (COREV2) from the Climate and Ocean - Variability, Predictability, and Change (CLIVAR project) (Large & Yeager, 2009). The atmospheric fields are displayed in a spatial grid of $1.9^{o}\times 2.5^{o}$, and the ocean/sea–ice models are set in $1.125^{o}\times 0.5^{o}$ spatial resolution in a displaced pole grid. The so-called normal year forcing (NYF) was used for the purpose of the sensitivity experiments. It constitutes of a 12-month climatology of the atmosphere fields relative to the period of 1948 to 2009 based on the NCEP/NCAR Reanalysis (Kalnay et al., 1996), which is then used to force the ocean model. Details of CORE2 forcing can be found at Large and Yeager (2009). The ocean model was integrated for 52 yr and the resulting simulation was used as a control run.

Sensitivity experiments were performed to understand how the formation of mode water in the South Atlantic responds to variations in surface fluxes. The climatological fields of precipitation rates (mm/day), downwelling shortwave radiation (W/m^2), and 10-m wind components (m/s) were amplified or reduced over the subtropical South Atlantic between 20°S to 50°S, with a gradual linear tapering toward those latitudes. Everywhere else outside the subtropical South Atlantic region, the climatological CORE2 fields remained unchanged (Figure S1).

The shortwave radiation experiments (SW) involved having their annual cycle increased (SW+) or decreased (SW-) by one standard deviation based on the CORE2 interannual forcing (IAF) from 1948 to 2009 (Figure S2). The precipitation experiments (PT) had their annual cycle increased by 25% (PT+) and reduced by 25% (PT-). This factor was determined to be as close as possible to a realistic change generated if we added/subtracted a standard deviation from the climatological value. In this way, all the modified area can increase or decrease uniformly, thus disregarding points with standard deviation greater than the average value. The wind speed experiments (WS) had a 10% (WS+) increase and a 10% (WS-) reduction in the annual cycle. This change was to both wind components (u and v) so that the direction was preserved and only the intensity was changed. The different rates applied to modify each of the variables (shortwave, precipitation and wind speed) do not introduce any type of bias or error in the analyses. We were not comparing the response of SASTMW formations between experiments, but between different types of SASTMW in each scenario.

2.2 Identification of mode water

To identify mode water we must combine two criteria: water columns with low PV (Equation 1), within a typical temperature range. For SASTMW, we identified layers with a PV less than 1.5×10^{-10} m^{-1} s^{-1} and the temperature range of 13°C to 16°C (Bernardo & Sato, 2020). We did not use the salinity range as a parameter for selecting SASTMW profiles because the amount of volume formed is more sensitive to the limits related to temperature (the selected range itself and its vertical gradient) and the vertical density variation, as we can see in the Text S2 (Figure S3 and Table S1). We also used a mixed layer depth (MLD) to compare with the thickness of the mode water profiles, that should be greater than the mean mixed layer depth. For ISAS data, we use an MLD climatology (J. Holte et al., 2010) and for SASTMW identified in the model outputs, the model's own estimated MLD (de Boyer Montégut et al., 2004).

The model outputs the variable PV as default, however it was not used for the identification because it contains other components such as the relative vorticity that is generally considered null for the study of mode waters. Thus, for both data sets, it was necessary to estimate the isopynic PV values (Suga & Hanawa, 1995), which disregards the relative vorticity and presents the following relationship:

$$PV = \frac{f}{\rho}\frac{\partial \rho}{\partial z}, \tag{1}$$

where f is the Coriolis parameter, ρ is potential density and z the depth vertical coordinate.

After selecting the profiles containing SASTMW, we applied a cluster analysis (Sato & Polito, 2014) to classify the mode water into three groups as a function of temperature, salinity, density and location. That division is important to evaluate each type of SASTMW independently and it was used in all subsequent analyzes.

3 Observed relationship between SASTMW and air-sea fluxes

In the first part of the study, we assess the observed relationship between the SASTMW formation and the air-sea interaction variables. For that we initially identify the mode water types in the region using the ISAS data. With that in hand, we can explore how mode water thickness co-varies with some aspects of the atmosphere and to evaluate any temporal delay between the air/sea layers.

The formation period begins in June and ends in November, with maximum values in September (Figure 1A.4). The annual cycle of mode water volume may vary over time. Generally the start and ending of mode water formation has the largest variations: June has the largest mode water volume coefficient of variation (standard deviation relative to the mean) considering the years covered by ISAS time series. The coefficient of variation in June is 258.6%; it drops to 35.9% in July; reduces to 21.1% in August; decreases to a minimum in September (13.7%); increases to 20.1% in October; and reaches the other maximum of 92.8% at the end of the cycle in November. As we can see, the greatest interannual variations do not occur at the peak of formation. That is, despite the differences observed in atmospheric processes and in the state of the ocean involved in the formation of the mode waters, in September the process of formation of the SASTMW tends to reach a stable level, slightly varying in relation to the average value. The largest variations in the mode water formation occur at the beginning and at the end of the season.

Thus, we focus our analysis on the months with the largest relative water volume STD, i.e. June, July and August (JJA). Figure 1 shows the grid point lagged correlation analysis between the 3-month mean atmospheric variables and the JJA mean thickness. To assess whether there is a difference in that relationship among the SASTMW types, we applied a cluster analysis (Subsection 2.2). The regions encompassing the three distinct SASTMW types during JJA are shown in Figure 2.

Among the ERA5 atmospheric variables, we use the surface net heat flux, evaporation minus precipitation (E–P) and wind speed at 10 m. The net heat flux includes the following components: upward latent, upward sensible, net upward longwave and net downward shortwave.

To match ISAS and ERA5 grid resolutions, we linearly interpolate the SASTMW thickness maps to the finer grid of 1/4°. The ERA5 atmospheric anomaly fields were then correlated with the ISAS thickness anomaly fields. The anomaly of the time series in each grid point was calculated by removing the mean annual cycle and applying a 13-month Blackman filter by convolution. Figure 1 exhibits the map of statistically significant correlation coefficients (p-value<0.05) per grid point and the mean annual cycle of each atmospheric variable averaged over the SASTMW type area.

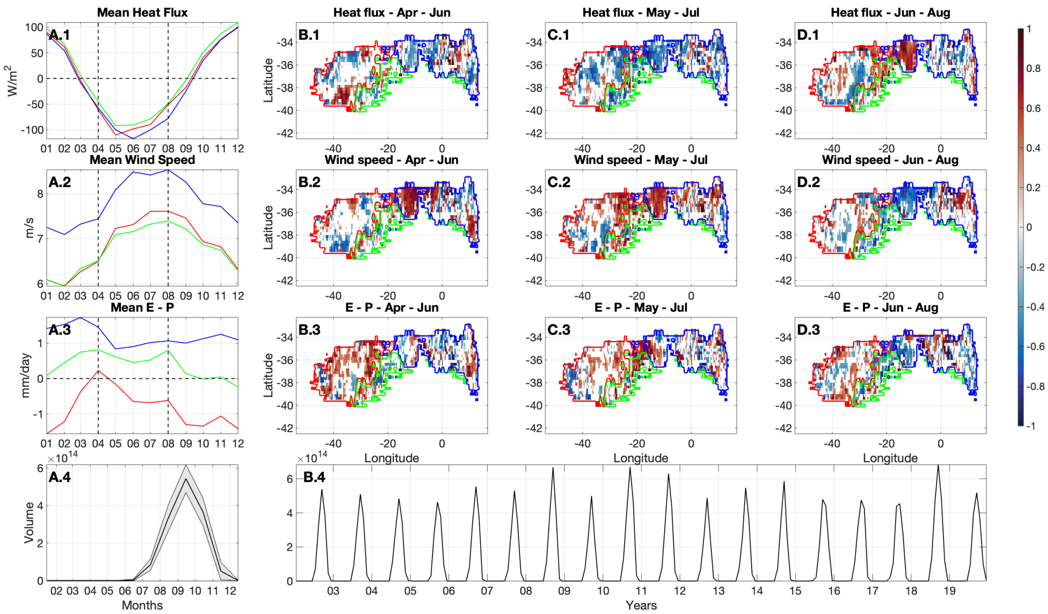

Figure 1. Column A: 2002-2009 mean annual cycle of the 1. net heat flux, 2. wind speed, and 3. evaporation minus precipitation, averaged over the area of each SASTMW type (see Figure 2A for reference). Maps (B–D): Grid point correlation coefficients between the June-to-August SASTMW volume anomaly and the atmospheric anomalies of 1. net heat flux, 2. wind speed, and 3. evaporation minus precipitation, during (Column B) April-to-June, (Column C) May-to-July, and (Column D) June-to-August. Only values statistically significant at the 95% level based on a Student t-test are shaded in columns B to D. Colors of the plot lines and contours: red (SASTMW1), blue (SASTMW2) and green (SASTMW3). Bottom panels: Climatology and standard deviation (grey shaded) (A.4), and monthly (B.4) volume of SASTMW on the surface between 2002 to 2019 from ISAS data.

From April to August the net heat flux in the South Atlantic subtropics is negative (Figure 1A1). Therefore, a negative correlation in Figure 1B–D1 means that the SASTMW thickness increases when the ocean loses heat. While the relationship between the SASTMW thickness and the Apr-Jun (Figure 1B1) net heat flux over the region is mainly weak and not spatially consistent, the May-Jul season (Figure 1C1) presents an overall negative correlation, and the Jun–Aug season (Figure 1D1) shows a reversed relationship. For the wind speed, a positive (negative) correlation represents an increase (decrease) of the mode water layer thickness. Since latent and sensible heat fluxes depend on wind speed, among other factors, the correlation patterns for wind speed are consistent with those from heat fluxes, but of opposite sign (Figure 1, panels B–D1 and B–D2).

Evaporation and precipitation impose different effects over the ocean: evaporation increases the density of the surface and can enhance the convection process (Talley et al., 2011) while precipitation reduces salinity and, thus, the surface density, stabilizing the water column (J. W. Holte et al., 2012). Consequently, for positive (negative) values of E-P, we expect an increase (decrease) in the density of the upper layers. This does not necessarily guarantee a change in SASTMW formation. This is due to the fact that each type of SASTMW has different typical density ranges. Therefore, the sign of the E-P variable can either contribute to an increase or a reduction in formation, in turn, related to the rates of water formation/destruction within these density ranges (Walin, 1982) and to the buoyancy flux (Gill, 1982; Donners et al., 2005). We also note that the

E–P shows different values between the different types of SASTMW (Figure 1A3). For SASTMW2 and 3, evaporation exceeds precipitation (E − P > 0, Figure 1A3)), so, the positive correlation indicates that there is an increase in thickness, linked to an increase in the convective process. For SASTMW1, we observed that precipitation values are on average higher than evaporation (E − P < 0, Figure 1A3), therefore, positive correlation means a decrease of the density values and a thickness decrease. We can see grid points with positive correlations mainly in the SASTMW1 region (Figure 1, panels B–C3).

The spatial correlation analysis show that the volume of SASTMW types respond significantly to variations in atmospheric variables. This statistical evidence in observations motivate us to explore further the processes for SASTMW formation using model simulations where atmospheric variables can be manipulated to impact the formation of the STMW in the South Atlantic.

4 Simulation of the SASTMW formation

The interest of the analysis was to examine an average year. Since the model forcing takes into account only the climatological year and there is an slight increasing tendency in the SASTMW formation (Figure S4), we used only the second run year of the control run to avoid that intrinsic increase in the model. We adopted the same choice of year for the sensitivity runs.

As a first approach, we evaluate the formation of SASTMW in the control run in response to the climatological atmospheric input data. Having an understanding of the formation process of each type of SASTMW, we assess the mode water response to the disturbances imposed in the sensitivity experiments.

4.1 SASTMW characteristics in the control run

The identified volume of SASTMW and the division between the three types present similar results to observations (Figure 1A4 and Figures 3–5G). Regarding the distribution of the average thickness per grid point, we note that the pattern is in accordance with Bernardo and Sato (2020), with the largest thicknesses concentrated in the northwestern portion of the surface layer, characterized by the presence of SASTMW1 (224±56 m). The remaining portions have lower values, with SASTMW2 having an average thickness of 163±62 m and SASTMW3 of 156±55 m.

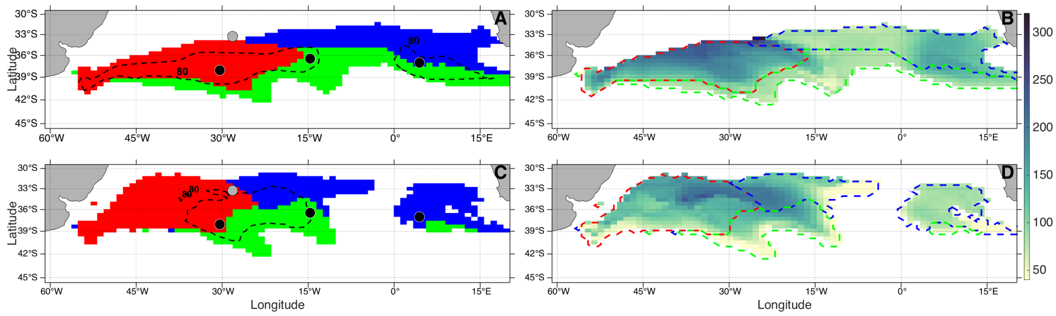

Figure 2. A: Average distribution of each type of SASTMW in the surface. Red: SASTMW1; Blue: SASTMW2; and Green: SASTMW3. Each black circle inside the SASTMW areas mark the point analyzed in Figure 3 to 5; the gray circle represents the point without mode water used in Figure 6. The area within the black dashed line encompasses 90% of mode water occurrence during winter. B: SASTMW surface average thickness and contour of selected isotherms. C: The same of the A, but for subsurface and with the occurrence rate during November to June. D: SASTMW subsurface average thickness. All maps were based in the daily output of the CESM model.

The identification of the different types of SASTMW allowed us to define reference points with the highest occurrence rate for each type and the region without mode water (circles in Figure 2). The description of what occurs in the upper layer of the ocean in the study region and the consequent formation process of the three types of SASTMW served as a basis for comparison with the results and changes of the developed sensitivity experiments (Section 4.2). By itself, the detailing of this process is already a great novelty for studies in the region and on the specific subject.

We selected three points of interest (Figure 2A) that presented 90% of the profiles containing mode water from July to October: The SASTMW1 profile is centered on 32.5°W, 37.5°S (Figure 3); SASTMW2, 4.5°E, 37°S (Figure 4); for SASTMW3, 17°E, 38°S (Figure 5). For comparison, we select one point without the presence of mode water located at 33.5°W, 28°S (Figure 6). Based on this selection, we describe the mode water formation process (Figures 3 to 5), in terms of its thermohaline characteristics, the stratification at each point and the relationship with the air-sea interface processes.

In the annual cycle of SASTMW1 the subsurface layer appears throughout the whole year (Figure 3E). We can see a gradual contraction of that layer from the beginning of the year until the end of May, outset of the formation process, presenting a thickness reduction of almost 25%. Until August, the lower limit of the layer remains stable, but we observe a more intense flattening from June to early August. The top of the subsurface layer is related to the sinking of the seasonal thermocline and the bottom to the position of the mean thermocline.

The beginning of the formation of SASTMW1 at this point occurs in mid June, when the 15.5°C isotherm appears at the surface. There is a continuous but shallow layer of very low PV (less than 2×10^{-11} m^{-1} s^{-1}) throughout May. We label this period as the "preconditioning phase" where the homogeneous surface layer begins to thicken, preparing the region for the formation process. Although the temperature is higher compared to the expected for the observed mode water, the ocean was already loosing heat to the atmosphere in that site since April (Figure 3C). That is why there was a shallow and very low PV mixed layer in April; thicker and more persistent than the warmer sea surface temperatures from January to March.

Although the ocean has been losing heat to the atmosphere during austral winter, the formed mode water layer remained separated from the subsurface layer by the seasonal thermocline (higher PV values in Figure 3E). During winter, precipitation increases, however, there is no visible effect in salinity, which also shows to increase in the surface layer. This is probably due to the fact that the surface wind strengthens since May, favoring evaporation and competing with the increased freshwater effect from precipitation to alter salinity. Thus, apparently, the positive precipitation anomaly does not seem to influence SASTMW1 as much, but instead wind speed and evaporation seem to play a larger role for salinity changes that lead to SASTMW1 formation. However, it is worth noting that SASTMW1 has the highest average salinity among the mode water types and the formation period was marked by an almost constant salinity (close to 35.5). According to Gordon (1981), the SASTMW1 formation region, close to the highly energetic BMC region, is marked by regional salinity maximum.

The thickening and sinking of the surface layer of SASTMW1 is related to a salinity increase and cooling from the beginning of the formation period until the rupture of the seasonal thermocline in mid-August (Figure 3C). After that, the subsurface layer becomes connected with the surface. From the beginning of the year until then, the SASTMW1 in subsurface presents greater stratification (compared to the surface layer in Figure 3E) but with low temperature vertical variation (Figure 3A). Due to this low gradient we estimate that the change in density, that intrinsically changes the PV, is related to the stratification observed in salinity (Figure 3B). The connection of the layers (Figure 3E) creates a window between the subsurface temperatures and the interface/surface characteristics.

Both low temperature and high salinity after the seasonal thermocline disruption come from the deeper layers. The loss of buoyancy in August and September coincides with the maximum positive anomaly of the wind speed (Figure 3F). These two effects together are sufficient for the layers of low PV (around 2×10^{-11} m^{-1} s^{-1}) to reach greater depths (J. W. Holte et al., 2012) (Figure 3E). The subsurface portion is ventilated not only during the mode waters formation process, but also after (Gordon, 1981; Rainville et al., 2014).

After October, the ocean starts to gain heat through the air–sea interface (Figure 3C) and the mode water layer becomes less homogeneous than when there was a clear connection with the interface. In mid-October, we noticed an increase of the stratification in the superficial portion and by November, there is a complete isolation of the SASTMW1 layer between the seasonal and main thermocline. Leaving aside the specifics, the process of formation and sinking of SASTMW1 is what we can consider as a standard explanation of the processes related to a mode water annual outcropping and subsurface establishment.

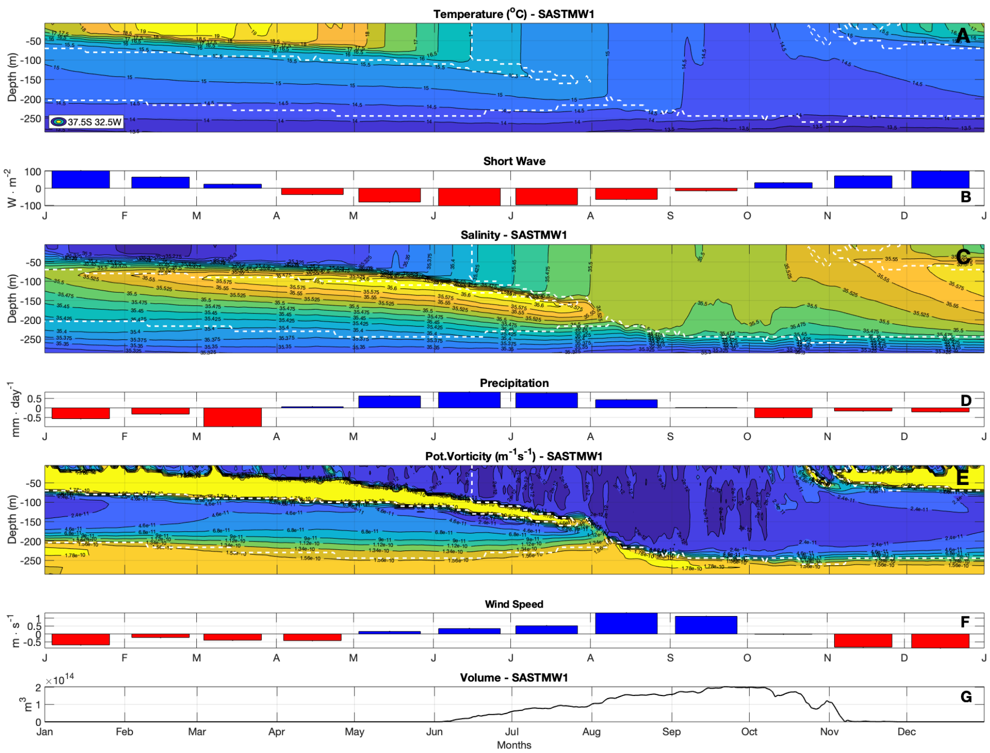

Figure 3. (A) Temperature, (B) shortwave radiation, (C) salinity, (D) precipitation, (E) potential vorticity, (F) wind speed, and (G) surface volume variation over one year at 37.5°S, 32.5°W in the CESM control run. The dashed white contours in (A), (C) and (E) represents the SASTMW 1 identified throughout the cycle. All the PV values greater than 1.5×10^{-10} m^{-1} s^{-1} were included in the maximum value contour.

In Figure 2 the region demarcated as SASTMW2 (blue region) hardly presents areas with occurrence above 90% in the surface (Figure 2A), during the winter, and it is nonexistent in the subsurface (Figure 2C). Because of that, we estimate that the formation of SASTMW2 usually occurs in a shorter period compared to SASTMW1 and it does not have a prolonged presence in the subsurface. This is another indicative that SASTMW2 have less persistence due to smaller thickness and more instability, typical of eastern mode water formations (Roemmich & Cornuelle, 1992). The instability can be seen in the enhancement of the temperature vertical gradient and the consequent increase of the PV vertical variation (compare Figure 4E to 3E and 5E). The mode water formation in that point starts later if compared to other types (Figure 4E), in mid-July, along with the increase in wind intensity in that region.

There is no formation nor disruption of a seasonal thermocline at the SASTMW2 reference point (Figure 4E), from the beginning of the year and the main thermocline appears to be shallower (compared to the others reference points). There is virtually no connection of the SASTMW layer formed at the surface with any pre-existing layer of mode water. Thus, there is no intrusion of colder waters from deeper layers and consequently, the SASTMW2 has the highest average temperature (15.0±0.6°C) among the three types. The higher mean temperature is probably due to the superficial introduction of relatively warmer waters (13°C to 18°C) through the Agulhas Retroflection (Olson et al., 1992). By the end of October, we note the increase of the stratification at the surface and the isolation of the SASTMW2 below that layer, but not as deep as the other types. The bottom of the mode water layer starts to increase the PV values in mid-September and at the end of November. This increment justifies why in Figure 2C we do not observe a high occurrence of mode waters in the eastern portion of the basin. We emphasize that SASTMW2 at this point does not respond much to variations in salinity and precipitation.

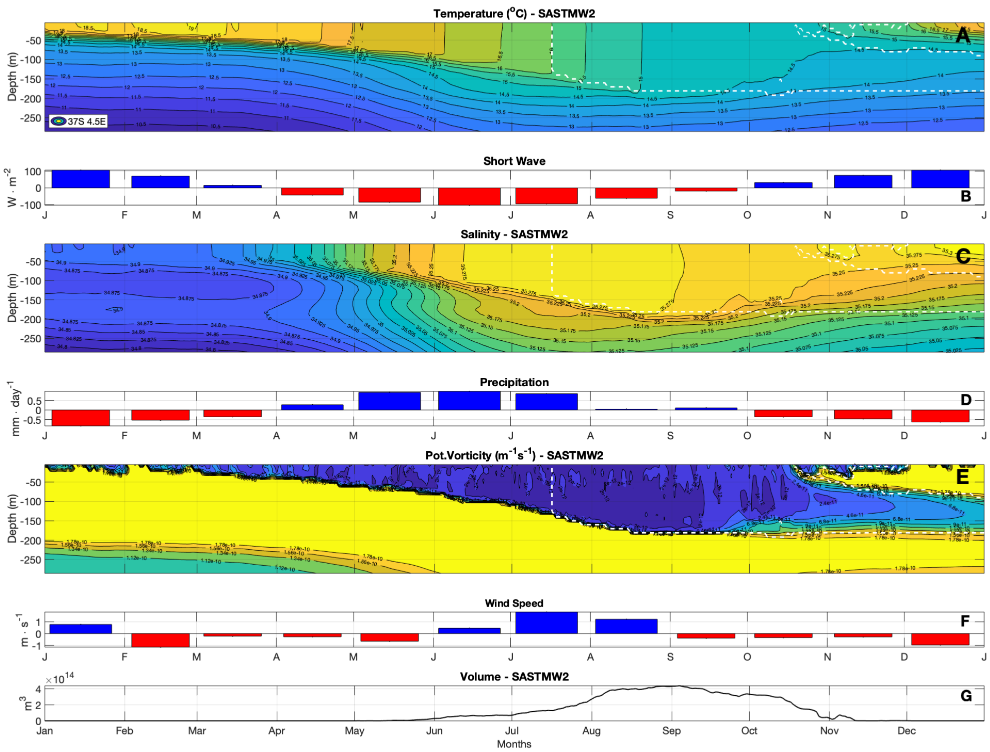

Figure 4. The same for the Figure 3, but at 37°S, 4.5°E and for SASTMW2.

SASTMW3 has annual cycle structure similar to that of SASTMW1 (compare Figure 3E and 5E). As in SASTMW1, SASTMW3 shows high occurrence rate (greater than 90 %) in both surface and subsurface layers (Figure 2A and C). The SASTMW3 formation starts before comparing with the other types (Figure 5E). SASTMW3 has the lowest average temperature (13.8±0.4°C), as a consequence of the formation region, which is farther south. We can also conclude that the preconditioning phase is shorter for the type 3. As it is spatially related to the South Atlantic Current (Stramma, 1989) and the STF (Legeckis & Gordon, 1982), the formation is influenced by colder central waters, which in turn receive volumetric contributions from Subantarctic Mode Water (McCartney, 1977; McCartney & Talley, 1982).

The seasonal thermocline in the SASTMW3 region persists until the end of August, therefore the connection of the surface and subsurface layers takes longer to occur compared to the other water types, and consequently the thickening period of the SASTMW3 is shorter (only in September). The surface–subsurface connection happens concomitantly with an increase in wind speed (August and September). The thickening process is limited by three factors: the persistence of the seasonal thermocline, the shallowing of cold isotherms and the stratification at the surface layers. Thus, PV values are not the main limitations for the identification of SASTMW3. The main thermocline at that point is deeper (above 250 m) among the three selected points. Thus, the homogeneous layer could be thicker and reach deeper isobates as much as the thermocline depth. The subsurface layer maintains a regular thickness around 100 m until July and because of the selection threshold of temperature, as the 13–isotherm elevates in depth, the same happens with the subsurface bottom layer. This is probably due to wind speed weakening after September (Figure 5F) and the increase of the shortwave radiation (Figure 5B), after which the convective process looses strength.

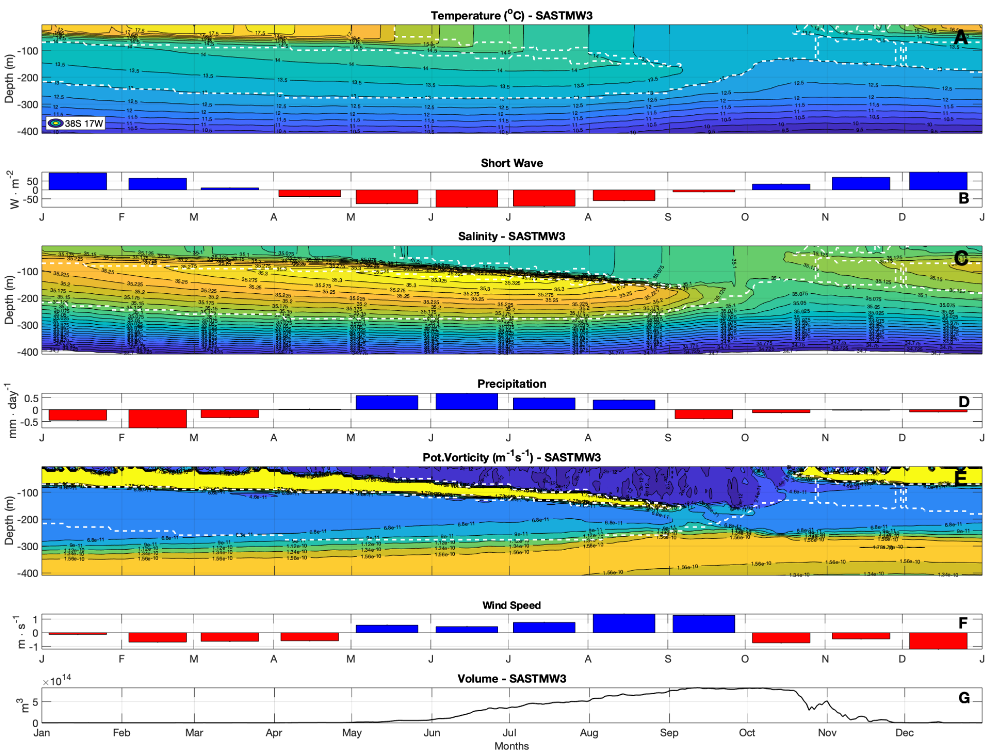

Figure 5. The same as Figure 3 but at 38° - 17°W and for SASTMW 3.

At the point without SASTMW formation, we can see that the 16°C isotherm barely outcrops (early October) during the typical formation period (Figure 6A). The strong stratification is indicative of the absence of mode water. In general, even if we select a broader temperature range, we would not see any subsurface isotherm outcropping at the surface. The salinity (Figure 5C) shows an homogeneous layer connected with the surface between 35.550 and 35.575. However, as observed in cases containing SASTMW, that does not seem to determine the formation of mode waters. The high PV values (Figure 5E) coincide with layers of low vertical temperature gradient. Therefore analyzing the temperature and the PV is enough for the determination of regions containing mode water.

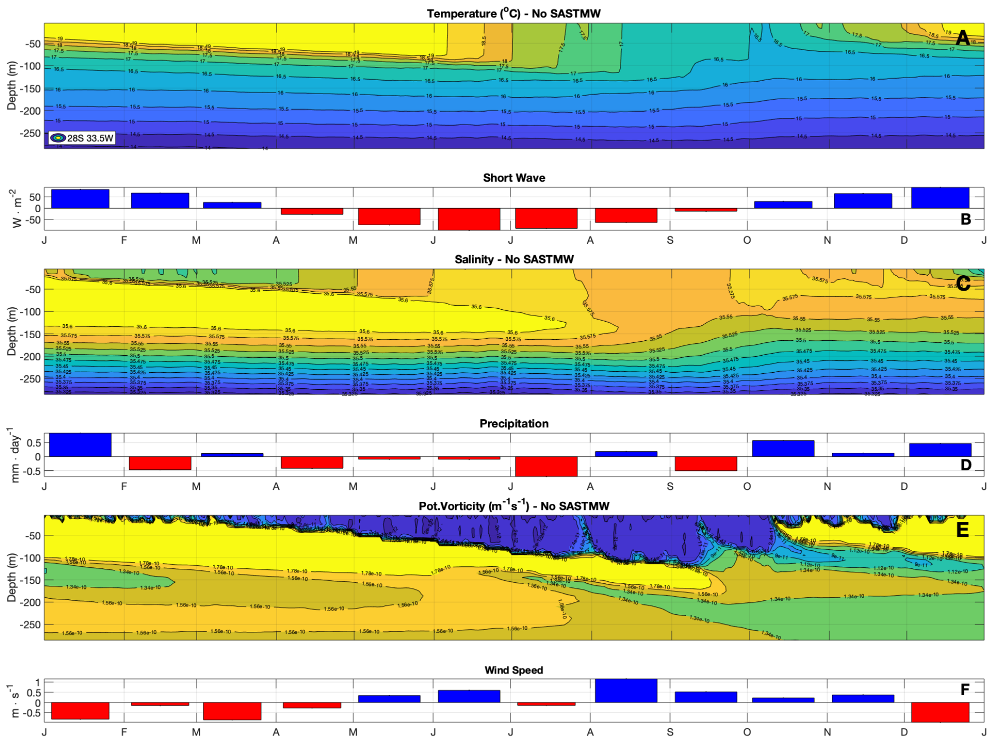

Figure 6. The same as Figure 3 but at 28°S, 33.5°W and without SASTMW of any type.

4.2 Simulated SASTMW in the sensitivity experiments

The sensitivity experiments were designed to understand how the formation of SASTMW would be impacted by different scenarios of atmospheric forcing. Six experiments were performed based on varying magnitudes of the climatological cycles of the following variables: shortwave radiation (SW), precipitation (PT), and wind speed (WS). The modification of the forcing is applied between the band of 33°S and 37°S (Figure S4) where most SASTMW forms. To the south and north of that band, there is a linear reduction of the atmospheric perturbation until it reaches its climatological values over a 20-degree latitude band.

To analyse the results of the sensitivity experiments, we use as reference the same cluster division and grid points assessed in the control run (Figures 3 to 5). It is important to note that the presence of mode water continued to occur in the selected points. The vertical sections similar to those made for the analysis of the control run are arranged in the Supplementary Material (Figures S5 to S22).

We present the results of changes in five SASTMW parameters: start date of mode water formation; date of mode water dissipation; average thickness; temperature; and PV during the winter period. Figure 7 shows the difference between the sensitivity experiments and the control run. Overall, we expect that an increase (decrease) in temperature is accompanied by a rise (reduction) in the PV values, and a shrink (thickening) of the mode water layer, due to strengthened (weaker) stratification. The higher (lower) stratification could delay (anticipate) the beginning of the formation and anticipate (postpone) the end of this process.

An increase (decrease) in the incidence of shortwave radiation would lead to a rise (reduction) in the ocean's temperature, which is not conducive for mode water formation. However, what draws our attention in the SW experiments is that, unlike the other types, the SASTMW3 thickness increases in SW+ (Figure 7C) and the SASTMW3 mean temperature rises in the SW- (Figure 7D) experiment. In the SW+, the 13°C isotherm, which is limiting for the selection of SASTMW and consequently mode water formation, is deeper than in the control run, thus allowing a greater thickening of warmer mode water layer at that point (compare Figure S17 and 5A for more details).

Regarding the thickness decrease of SASTMW3 in the SW-, we observed the opposite effect. The reduction in the incidence of shortwave radiation causes a cooling of the ocean and instead of the outcrop of waters between 13°C and 13.5°C on the surface (Figure 5A), the emergence of colder waters out of identification threshold occur. Despite this, the average temperature increases (Figure 7D). This is related to the fact that the formation of SASTMW3 is interrupted almost two months earlier (Figure 7B) and only profiles until the beginning of September are considered, a period with warmer surface isotherms, compared to the isotherms on the surface of the control run during the formation period (compare Figure 5A and S18 for more details).

It is known that precipitation can alter mixing in the upper ocean (Moum & Smyth, 2001). If precipitation (evaporation) is greater than evaporation (precipitation), the surface of the ocean loses (gains) buoyancy, the effect being similar to the ocean been heated (cooled) (Cronin & Sprintall, 2009). Rainfall can isolate turbulence in the surface generated by winds, reducing the vertical mixing and the influence of the surface forcing to the subsurface. On the other hand, if evaporation is superior to precipitation, convection can be intensified (Moum & Smyth, 2001). Therefore, in the PT experiments, (Figure S7, S8, S13, S14, S19 and S20) the "evaporation - precipitation" relationship is altered, inverting the signal, reducing or intensifying the difference. In PT+, the convective mixing process in the upper layers of the ocean de-intensifies or even paralyzes. In PT-, the reverse occur and the response of the ocean in these experiments is directly consistent with the SW scenarios. Thus, we highlight, comparing to the others types, that there is an anomalous inversion of the mean PV SASTMW2 in both experiments (Figure 7E, PT+ and PT-), although the similar variation in temperature. This is an indication that the formation of SASTMW2 is more affected by dynamic processes.

Despite the relationship between the wind speed, net heat flux, and the evaporation processes (Talley et al., 2011), the dynamic effect of the wind on the formation of mode water presents a greater response from the upper ocean. Winds generate an important mixing affecting the temperature in the upper ocean (J. W. Holte et al., 2012). Wind drives the Ekman transport which has a fundamental role in the interannual variations of the mode water volume (Sloyan et al., 2010). As we increase the intensity of the wind (WS+), the average temperature and PV of the SASTMW layer decreases (Figure 7) due to the strengthening of the vertical mixing and the ventilation of the upper layer of the oceans with deeper and colder waters. The wind reduction in the WS- has an inversely proportional effect on the average temperature and an inverse result in PV values. The reduction in thickness (Figure 7C) of SASTMW3 in WS+ is due to a process similar to that of the SW- (compare Figure S18 and S21 for more details), and the inversion of the signals in relation to the beginning day of SASTMW1 and SASTMW3 formation (Figure 7A) is merely due to appearance of the 16°C isotherm at the surface.

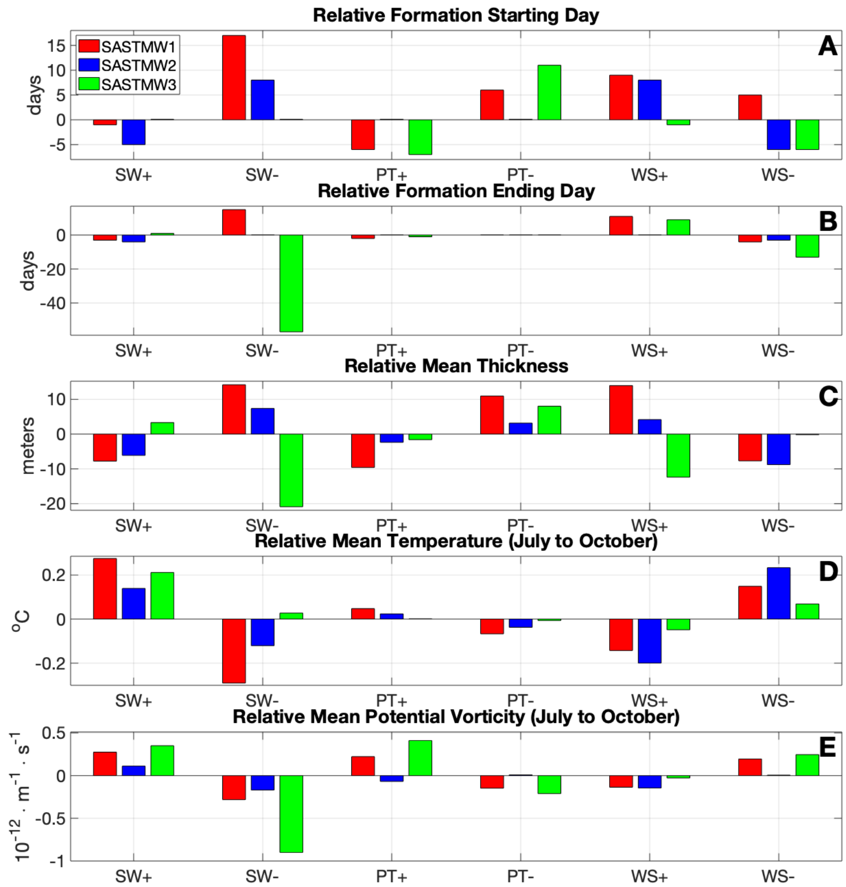

Figure 7. Simulated mode water response to one standard deviation (±) increase and decrease of shortwave input values (SW+ and SW-); ±25% intensification and reduction in precipitation (PT+ and PT-); and, ±10% rise and weakening in wind speed (WS+ and WS-). All the variables are relative to the control run (sensitivity experiment minus control run). Red: SASTMW1. Blue: SASTMW2. Green: SASTMW3. (A) Positive (negative) values represent the advance (delay) of the formation. (B) Negative (positive) values represent the advance (delay) of the formation end. (C) Relative mean thickness. (D) Relative Mean temperature response from July to October. (E) Relative mean potential vorticity from July to October.

With a better understanding of the relationship between the formation of SASTMW and variables in the different experiments and the particularities observed in the Figure 7, we can evaluate the changes generated by the scenarios of the experiments in a broader way. Therefore, we further investigate the response of SASTMW through 5 parameters: mean volume, area, thickness, ocean heat storage (OHS) and STMW intensity anomaly (Figure 8). The volume quantifies how much the SASTMW formations are impacted in each scenario and being the volume a function of the area and thickness, we can determine if this change is affected more horizontally or vertically. The OHS is directly related to the temperature and it is a diagnosis of how much the ocean is heated or cooled vertically. The STMW intensity (I), estimated via a PV threshold (1.5×10^{-10} m^{-1} s^{-1}) as a reference, allows us to assess the homogeneity of each profile (Text S3) (Qiu et al., 2006) (McCartney & Talley, 1982). If I is negative (positive), the profiles are more (less) stratified than the control. Figure 8 shows the results for each variable of the sensitivity experiments relative to the control.

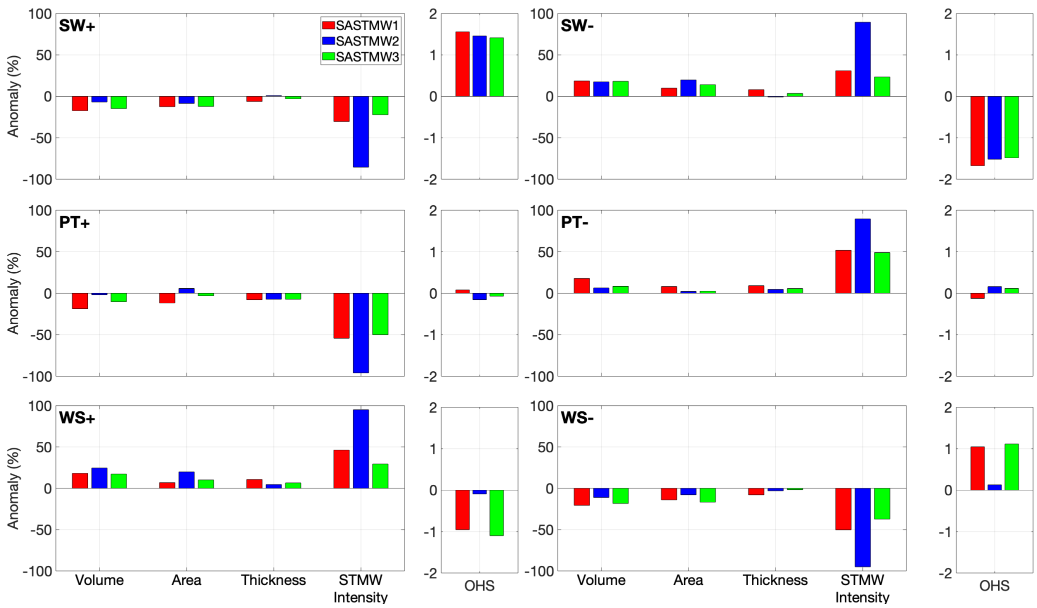

Figure 8. Mean winter mode water volume, area, thickness, intensity, and ocean heat storage (OHS) relative to the control run for each SASTMW type in each sensitivity experiment run.

Overall, SASTMW2 intensity is more sensitive than SASTMW1 and 3 to changes in the atmospheric forcing in all experiments (Figure 8). This is possibly due to the fact that the SASTMW2 region (Figure 9) already presents negative I values during winter (-6.8$\times 10^{-9}$ s^{-1}). This result is in line with the fact that the eastern subtropical portion of the South Atlantic has less stable water columns (more stratified) (Roemmich & Cornuelle, 1992; Bernardo & Sato, 2020). That instability is due to the proximity to the Agulhas Retroflection which is known as a highly energetic region (Olson & Evans, 1986). Although mode waters can be formed in the retroflection (South Indian STMW) (Olson et al., 1992) resulting from the remaining winter mixed layer of the Indian Ocean, these formations are more stratified than the mode waters observed in the western South Atlantic or in the Northern Hemisphere (Toole & Warren, 1993; Hanawa & Talley, 2001). Thus, in experiments where there is a tendency to increase ocean stratification, regions that are already vertically unstable are predisposed to amplify this response.

Unstable regions usually have negative I values. In experiments where there is a tendency to increase homogeneity of the surface layer, the values of I become positive. Thus, the increase in SASTMW2 intensity stands out in relation to other types (Figure 8). Following that logic, we note that the volume anomaly of SASTMW2 was greater in magnitude when the ocean became more homogeneous than when it was more stratified. In other words, the volume of SASTMW2 is way more affected by processes that increase the homogeneity of the column than the reverse.

As expected, changes in the incidence of shortwave radiation (SW experiments) show the greatest effect on the OHS values, with a slight difference between the types. However, that difference is not directly proportional to the volume. For SASTMW1, the changes in the SW+ case is double the changes in thickness, and in SW- that relationship is very well balanced. This is because region 1 loses more heat in SW- than it gains in SW+, vertically altering the ocean more effectively.

Although the three types of SASTMW presented a similar response in relation to the heat storage in both SW experiments (SW+ and SW-), only SASTMW2 had an almost exclusive association of the change in volume with the variation in the area occupied by the mode water, with less than ±1% variation in thickness, i.e. virtually no gain or loss of thickness. That is, the volume was altered by the addition or reduction of profiles considered sufficiently homogeneous to be labeled as subtropical mode waters. For SASTMW3, there is a more pronounced variation of the area, however, changes in thickness should be considered for the volume alterations. The increase in area was related to greater profiles associated with the cooler temperatures linked to the typical SASTMW and the thickness variation, to the vertical position of the 13°C isotherm.

Figure 9B shows that SASTMW1 is related to the highest precipitation values (4.0±0.5 mm/day), justifying that the volume of SASTMW1 was the most impacted by the changes imposed by the experiments. The opposite can be observed in relation to region 2, where there is a distribution of the lowest precipitation values (2.7±1.0 mm/day) among the areas and the least impact on the volume. The thickness anomaly was similar between the three types of SASTMW (Figure 8 PT+). Therefore, what determines the difference in volume among them is the anomaly of the area, with SASTMW1 being the most negatively affected. The increase in precipitation in a region that already has higher values reduces the freshwater flux more vehemently, decreasing the amount of profiles containing STMW. In the PT-, both the thickness and area anomaly of the SASTMW1 are highest, however, what differentiates the impact on the volume of SASTMW2 and 3 is the increase in thickness. The same logic applied previously to the freshwater flux explains the relationship obtained in this experiment.

Yet, observing the low variation of the OHS, we understand that the influence of precipitation is almost exclusively dynamic. Even though the signal of the heat storage of the SASTMW1 is inverted compared to other types, there is no proportional effect on the volume anomaly (Figure 8). However, in the PT+, we observed that the volume of SASTMW2 practically did not vary (-1.8%). That effect was related to an increase of the occupied area as opposed to a reduction in thickness. Therefore, despite the expected reduction in average thickness, the increase in precipitation in an area with low rate reduced the heat storage and altered the salinity of region 2, horizontally adding profiles that were previously not considered SASTMW2.

The temperature variation is the inverse of WS experiment sign, and the same can be seen in the OHS (Figure 7D). Nevertheless, the stratification of the SASTMW2 is more affected than the OHS, when compared with the other types. The formation of SASTMW2 is influenced by the Agulhas Retroflection which in addition to introducing turbulent energy into the South Atlantic (Olson & Evans, 1986), injects relatively saltier and warmer water, thus representing a significant heat input into the South Atlantic system (Gordon, 1985). In the eastern portion of the South Atlantic, we assume that the inflow of water from the Indian Ocean has more influence on the heat storage than the winds over that region. According to Bernardo and Sato (2020), there is another factor that influences the SASTMW2 formation rate in addition to the heat flux, and the amount of heat transferred between the basins should be considered as a possibly factor. The influence of the wind on this process is in the relation of the latitudinal position of the Southern Hemisphere westerlies with the increase in the Agulhas Leakage (Biastoch et al., 2009), and not necessarily with the intensity of the winds, a factor altered in the experiments.

Another relationship that is noteworthy is that with the increase in the WS+, SASTMW1 has a greater gain in thickness and SASTMW3 in area. It becomes evident when we look at Figure 9C where region 1 has higher wind wave values in magnitude than region 3, so with increasing intensity of wind components, vertical pumping can be intensified downwards and thickness tends to increase. The distance between the cooler isotherms linked to SASTMW3 increases, and consequently the area as well. This being related to the direction and intensity of the winds observed in Figure 9D, such like the results for the same type in the SW+. The opposite process happens for the SASTMW3 in the WS- . In that one, the SASTMW1 region gains more heat and becomes more stratified than the opposite in the WS+. Therefore, the effect becomes similar to what occurs in the SW+.

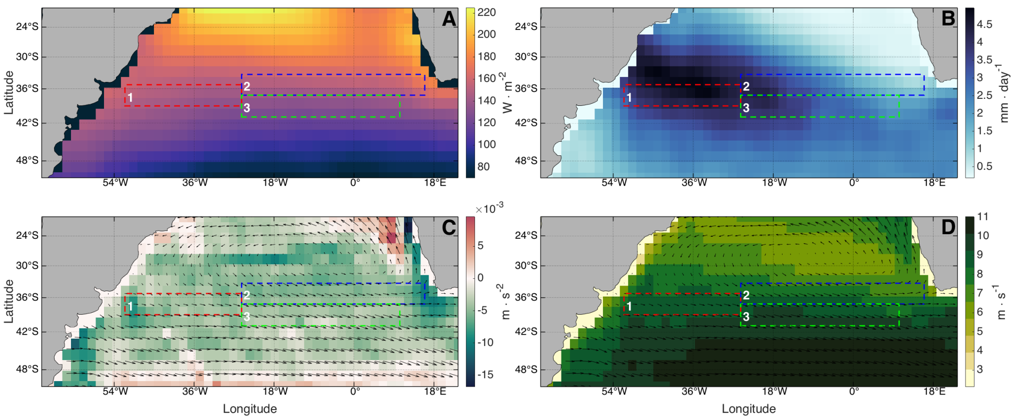

Figure 9. Annual mean maps for the South Atlantic of the NCAR–CESM model input data. A. Surface Downwelling Shortwave Flux; B. Precipitation; C. Calculated wind curl (colors) and wind vector; D. Calculated wind speed (colors) and wind vector. Red box (1): SASTMW1; blue box (2): SASTMW2; green box (3): SASTMW3.

5 Conclusions

We evaluated the relationship between the formation of different types of South Atlantic Subtropical Mode Water with different processes at the air-sea interface. In addition, we assessed whether there is a distinct response from each type of SASTMW to a given process. Significant correlation was observed between the SASTMW types from ISAS and the air-sea interaction variables of surface net heat flux, precipitation, evaporation, and wind speed from the ERA5. That result motivated us to evaluate the formation of SASTMW in a general circulation model (NCAR CESM1.2.2), where we could control the intensity of the atmospheric forcing to understand the response in the mode water characteristics.

The control run simulated the general features of the SASTMW with high degree of fidelity and allowed us to evaluate each mode water type separately and to explore the particularities of each formation process. Each mode water type presents distinct thermohaline composition, different formation cycles, outcrop periods and vertical stratification structures. Thus, giving us a hint that each formation should have a different relationship with the processes at the interface. Sensitivity experiments were designed where the intensity of the shortwave radiation, precipitation and wind components magnitude could be amplified or reduced.

The SASTMW1 showed an increase in volume compared to the control for WS+, SW- and PT-, with values close to each other (i.e. 18.2±0.4%). When the volume is reduced, SASTMW1 suffers the greatest impact with changes in the intensity of the winds and is less sensitive to the shortwave incidence increase. The variation in volume of the SASTMW2 has a very low relationship with precipitation, having a greater relationship with the variation in wind intensity, particularly for wind intensification. Therefore, dynamical processes have greater influence on this mode water. The anomaly of the SASTMW3 volume has a lower rate in the precipitation experiments when compared to the others. If we evaluate the SW and WS experiments, we note that the SASTMW3 is the least impacted in terms of the stratification of the region, the area is always more affected than the thickness. Therefore, SASTMW3 is more influenced by the greater or lesser availability of water in lower temperatures (in relation to the observation limit of SASTMW). Because it is a region with relatively lower heat loss, that input must come from the southernmost portion of the South Atlantic related to the Subantartic Mode Water (Tsuchiya, 1986) or a cross-frontal transport (Smythe-Wright et al., 1998).

In summary, our study provided insights onto air-sea processes for the formation of mode water in the South Atlantic. We conclude that variations in the volume of SASTMW1 and 3 are primarily driven by changes in thermodynamical processes, while the formation of SASTMW2 is mostly influenced by dynamical processes.

Acknowledgments

We acknowledge the use of the following datasets: ISAS-15 temperature and salinity products were produced and distributed by the French Service National d'Observation Argo at LOPS and are available at https://doi.org/10.17882/52367. ISAS-NRT is available at http://marine.copernicus.eu/services-portfolio/access-to-products. ERA–5 (Copernicus Climate Change Service (C3S), 2017) is available at https://doi. org/10.5065/D6X34W69. We are grateful to the institutions listed below for the direct or indirect support that they are providing us: Process 141822/2017-1, National Council for Scientific and Technological Development (CNPq), University of So Paulo (USP), Climate Change Research Centre of the University of New South Wales (CCRC–UNSW). The numerical experiments were performed at the National Computing Infrastructure Facility, Australia. This study is linked to projects 2015/26450-8 and 2015/50324-2 funded by Fundao de Amparo Pesquisa do Estado de So Paulo (FAPESP). The Australian Research Council supported A.S.T. (FT160100495).

References

Beal, L. M., De Ruijter, W. P., Biastoch, A., Zahn, R., et al. (2011). On the role of the Agulhas system in ocean circulation and climate. *Nature*, *472*(7344), 429–436.

Bernardo, P. S., & Sato, O. T. (2020). Volumetric Characterization of the South Atlantic Subtropical Mode Water Types. *Geophysical Research Letters*, *47*(8), e2019GL086653.

Biastoch, A., Böning, C. W., Schwarzkopf, F. U., & Lutjeharms, J. (2009). Increase in Agulhas leakage due to poleward shift of Southern Hemisphere westerlies. *Nature*, *462*(7272), 495.

Cronin, M., & Sprintall, J. (2009). Wind and buoyancy-forced upper ocean. *Elements of Physical Oceanography: A derivative of the Encyclopedia of Ocean Sciences*, 237–245.

Deacon, S. G. E. R., & Britain, G. (1937). *Note on the dynamics of the Southern Ocean*. University Press.

de Boyer Montégut, C., Madec, G., Fischer, A. S., Lazar, A., & Iudicone, D. (2004). Mixed layer depth over the global ocean: An examination of profile data and a profile-based climatology. *Journal of Geophysical Research*, *109*(C12), C12003.

Dong, S., & Kelly, K. A. (2013). How Well Do Climate Models Reproduce North Atlantic Subtropical Mode Water? *Journal of Physical Oceanography*, *43*(10), 2230–2244.

Donners, J., Drijfhout, S., & Hazeleger, W. (2005). Water mass transformation and subduction in the South Atlantic. *Journal of Physical Oceanography*, *35*(10), 1841–1860.

Douglass, E. M., Jayne, S. R., Peacock, S., Bryan, F. O., & Maltrud, M. E. (2012). Subtropical mode water variability in a climatologically forced model in the northwestern pacific ocean. *Journal of Physical Oceanography*, *42*(1), 126–140.

Douglass, E. M., Kwon, Y.-O., & Jayne, S. R. (2013). A comparison of North Pacific and North Atlantic subtropical mode waters in a climatologically-forced model. *Deep Sea Research Part II: Topical Studies in Oceanography*, *91*, 139–151.

Duncombe Rae, C. M. (1991). Agulhas retroflection rings in the South Atlantic Ocean: an overview. *South African Journal of Marine Science*, *11*(1), 327–344.

Escoffier, C., & Provost, C. (1998). Surface forcing over the South West Atlantic according to NCEP and ECMWF reanalyses over the period 1979–1990. *Physics and Chemistry of the Earth*, *23*(5), 537–542.

Ferreira, M., Sato, O., Polito, P., & Bernardo, P. (2019). Examining the Subtropical Mode Water in the Southwestern Atlantic From in Situ Observations. *Journal of Geophysical Research: Oceans*, *124*(4), 2513–2526.

Fine, R. A., Warner, M. J., & Weiss, R. F. (1988). Water mass modification at the agulhas retroflection: Chlorofluoromethane studies. *Deep Sea Research Part A. Oceanographic Research Papers*, *35*(3), 311–332.

Gaillard, F., Reynaud, T., Thierry, V., Kolodziejczyk, N., & von Schuckmann, K. (2016). In situ–based reanalysis of the global ocean temperature and salinity with ISAS: Variability of the heat content and steric height. *Journal of Climate*, *29*(4), 1305–1323.

Garzoli, S. L., & Bianchi, A. (1987). Time-space variability of the local dynamics of the Malvinas-Brazil confluence as revealed by inverted echo sounders. *Journal of Geophysical Research: Oceans*, *92*(C2), 1914–1922.

Garzoli, S. L., & Garraffo, Z. (1989). Transports, frontal motions and eddies at the Brazil-Malvinas Currents Confluence. *Deep Sea Research Part A. Oceanographic Research Papers*, *36*(5), 681–703.

Gill, A. E. (1982). *Atmosphere-Ocean dynamics (International Geophysics Series).* Academic Press.

Gordon, A. L. (1981). South Atlantic thermocline ventilation. *Deep Sea Research Part A. Oceanographic Research Papers*, *28*(11), 1239–1264.

Gordon, A. L. (1985). Indian-Atlantic transfer of thermocline water at the Agulhas Retroflection. *Science*, *227*(4690), 1030–1033.

Gordon, A. L., & Greengrove, C. L. (1986). Geostrophic circulation of the Brazil-Falkland confluence. *Deep Sea Research Part A. Oceanographic Research Papers*, *33*(5), 573–585.

Hanawa, K., & Talley, L. (2001). 4. Mode waters. *International Geophysics*, *77*, 373–386.

Hazeleger, W., & Drijfhout, S. (1998). Mode water variability in a model of the subtropical gyre: Response to anomalous forcing. *Journal of Physical Oceanography*, *28*(2), 266–288.

Hersbach, H., Bell, W., Berrisford, P., Horányi, A., Joaquí, M., Nicolas, J., . . . others (2019). Global Reanalysis: Goodbye ERA-Interim, Hello ERA5. *ECMWF Newsl*, *159*, 17–24.

Holte, J., Talley, L. D., Gilson, J., & Roemmich, D. (2010). Argo mixed layers. *Scripps Institution of Oceanography/UCSD*.

Holte, J. W., Talley, L. D., Chereskin, T. K., & Sloyan, B. M. (2012). The role of air-sea fluxes in Subantarctic Mode Water formation. *Journal of Geophysical Research: Oceans*, *117*(C3).

Hosoda, S., Takeuchi, K., Xie, S.-P., & Nonaka, M. (2001). Eastern North Pacific Subtropical Mode Water in a general circulation model - Formation mechanism and salinity effects. *Journal of Geophysical Research*, *106*, 19671–19681.

Hurrell, J. W., Holland, M. M., Gent, P. R., Ghan, S., Kay, J. E., Kushner, P. J., ... others (2013). The community earth system model: a framework for collaborative research. *Bulletin of the American Meteorological Society*, *94*(9), 1339–1360.

Joyce, T. M., Thomas, L. N., Dewar, W. K., & Girton, J. B. (2013). Eighteen degree water formation within the Gulf Stream during CLIMODE. *Deep Sea Research Part II: Topical Studies in Oceanography*, *91*, 1–10.

Kalnay, E., Kanamitsu, M., Kistler, R., Collins, W., Deaven, D., Gandin, L., ... others (1996). The NCEP/NCAR 40-year reanalysis project. *Bulletin of the American meteorological Society*, *77*(3), 437–472.

Kay, J., Deser, C., Phillips, A., Mai, A., Hannay, C., Strand, G., ... others (2015). The Community Earth System Model (CESM) large ensemble project: A community resource for studying climate change in the presence of internal climate variability. *Bulletin of the American Meteorological Society*, *96*(8), 1333–1349.

Kelly, K. A., & Dong, S. (2013). The contributions of atmosphere and ocean to North Atlantic Subtropical Mode Water volume anomalies. *Deep Sea Research Part II: Topical Studies in Oceanography*, *91*, 111–127.

Kolodziejczyk, N., Prigent-Mazella, A., & Gaillard, F. (2017). *ISAS-15 temperature and salinity gridded fields.* SEANOE. Retrieved from `https://www.seanoe.org/data/00412/52367/` doi: 10.17882/52367

Kouketsu, S., Tomita, H., Oka, E., Hosoda, S., Kobayashi, T., & Sato, K. (2011). The role of meso-scale eddies in mixed layer deepening and mode water formation in the western North Pacific. In *New Developments in Mode-Water Research* (pp. 59–73). Springer.

Large, W., & Yeager, S. (2009). The global climatology of an interannually varying air–sea flux data set. *Climate dynamics*, *33*(2-3), 341–364.

Legeckis, R., & Gordon, A. L. (1982). Satellite observations of the Brazil and Falkland currents - 1975 to 1976 and 1978. *Deep Sea Research Part A. Oceanographic Research Papers*, *29*(3), 375–401.

Li, Z. (2012). Interannual and decadal variability of the subtropical mode water formation in the South Pacific Ocean. *Ocean Modelling*, *47*, 96–112.

Masuzawa, J. (1969). Subtropical mode water. *Deep Sea Research and Oceanographic Abstracts*, *16*(5), 463–472.

Maze, G., Deshayes, J., Marshall, J., Tréguier, A.-M., Chronis, A., & Vollmer, L. (2013). Surface vertical PV fluxes and subtropical mode water formation in an eddy-resolving numerical simulation. *Deep Sea Research Part II: Topical Studies in Oceanography*, *91*, 128–138.

McCartney, M. S. (1977). Subantarctic mode water. *A Voyage of Discovery: George Deacon 70th Anniversary Volume*, 103–119.

McCartney, M. S., & Talley, L. D. (1982). The subpolar mode water of the North Atlantic Ocean. *J. Phys. Oceanogr*, *12*(11), 1169–1188.

Moum, J., & Smyth, W. (2001). Upper ocean mixing processes. *Encyclopedia of Ocean Sciences*, *6*, 3093–3100.

Oka, E., & Qiu, B. (2012). Progress of North Pacific mode water research in the past decade. *Journal of Oceanography*, *68*(1), 5–20.

Olson, D. B., & Evans, R. H. (1986). Rings of the Agulhas current. *Deep Sea Research Part A. Oceanographic Research Papers*, *33*(1), 27–42.

Olson, D. B., Fine, R. A., & Gordon, A. L. (1992). Convective modifications of water masses in the Agulhas. *Deep Sea Research Part A. Oceanographic Research Papers*, *39*, S163–S181.

Peng, G., Chassignet, E. P., Kwon, Y.-O., & Riser, S. C. (2006). Investigation of variability of the North Atlantic Subtropical Mode Water using profiling float data and numerical model output. *Ocean Modelling*, *13*(1), 65–85.

Peterson, R. G., & Stramma, L. (1991). Upper-level circulation in the South Atlantic Ocean. *Progress in Oceanography*, *26*(1), 1–73.
Pezzi, L. P., Souza, R. B. d., Dourado, M. S., Garcia, C. A. E., Mata, M., & Silva-Dias, M. (2005). Ocean-atmosphere in situ observations at the Brazil-Malvinas Confluence region. *Geophysical Research Letters*, *32*(22).
Provost, C., Escoffier, C., Maamaatuaiahutapu, K., Kartavtseff, A., & Garçon, V. (1999). Subtropical mode waters in the South Atlantic Ocean. *Journal of Geophysical Research-Oceans*, *104*(C9), 21,033–21,049.
Qiu, B., & Chen, S. (2006). Decadal variability in the formation of the North Pacific Subtropical Mode Water: Oceanic versus atmospheric control. *Journal of Physical Oceanography*, *36*(7), 1365–1380.
Qiu, B., Chen, S., & Hacker, P. (2007). Effect of mesoscale eddies on subtropical mode water variability from the Kuroshio Extension System Study (KESS). *Journal of Physical Oceanography*, *37*(4), 982–1000.
Qiu, B., Hacker, P., Chen, S., Donohue, K. A., Watts, D. R., Mitsudera, H., … Jayne, S. R. (2006). Observations of the subtropical mode water evolution from the Kuroshio Extension System Study. *Journal of Physical Oceanography*, *36*(3), 457–473.
Rainville, L., Jayne, S. R., & Cronin, M. F. (2014). Variations of the North Pacific subtropical mode water from direct observations. *Journal of Climate*, *27*(8), 2842–2860.
Rainville, L., Jayne, S. R., McClean, J. L., & Maltrud, M. E. (2007). Formation of subtropical mode water in a high-resolution ocean simulation of the Kuroshio Extension region. *Ocean Modelling*, *17*(4), 338–356.
Rintoul, S. R., & England, M. H. (2002). Ekman transport dominates local air–sea fluxes in driving variability of Subantarctic Mode Water. *Journal of Physical Oceanography*, *32*(5), 1308–1321.
Roemmich, D., & Cornuelle, B. (1992). The subtropical mode waters of the South Pacific Ocean. *Journal of Physical Oceanography*, *22*(10), 1178–1187.
Sato, O., & Polito, P. (2014). Observation of South Atlantic subtropical mode waters with Argo profiling float data. *Journal of Geophysical Research: Oceans*, *119*(5), 2860–2881.
Silveira, I. C. A. d., de Miranda, M. B., & Brown, W. S. (1994). On the origins of the North Brazil Current. *J. Geophys. Res.*, *99*, 22501-22512.
Sloyan, B. M., Talley, L. D., Chereskin, T. K., Fine, R., & Holte, J. (2010). Antarctic Intermediate Water and Subantarctic Mode Water formation in the Southeast Pacific: The role of turbulent mixing. *Journal of Physical Oceanography*, *40*(7), 1558–1574.
Smythe-Wright, D., Chapman, P., Duncombe Rae, C. M., Shannon, L. V., & Boswell, S. M. (1998). Characteristics of the South Atlantic subtropical frontal zone between 15°W and 5°E. *Deep Sea Research Part I: Oceanographic Research Papers*, *45*(1), 167–192.
Stramma, L. (1989). The Brazil Current transport south of 23°S. *Deep Sea Research Part A. Oceanographic Research Papers*, *36*(4), 639–646.
Stramma, L., & Peterson, R. G. (1989). Geostrophic transport in the Benguela Current region. *Journal of Physical Oceanography*, *19*(10), 1440–1448.
Stramma, L., & Peterson, R. G. (1990). The South Atlantic Current. *Journal of Physical Oceanography*, *20*(6), 846–859.
Suga, T., & Hanawa, K. (1995). The subtropical mode water circulation in the North Pacific. *Journal of Physical Oceanography*, *25*(5), 958–970.
Talley, L. D. (1999). Some aspects of ocean heat transport by the shallow, intermediate and deep overturning circulations. *Geophysical Monograph-American Geophysical Union*, *112*, 1–22.
Talley, L. D., Pickard, G. L., Emery, W. J., & Swift, J. H. (2011). *Descriptive physical oceanography: an introduction.* Access Online via Elsevier.

Toole, J. M., & Warren, B. A. (1993). A hydrographic section across the subtropical South Indian Ocean. *Deep Sea Research Part I: Oceanographic Research Papers*, *40*(10), 1973–2019.

Tsuchiya, M. (1986). Thermostads and circulation in the upper layer of the Atlantic Ocean. *Progress in Oceanography*, *16*(4), 235–267.

Tsuchiya, M., Talley, L. D., & McCartney, M. S. (1994). Water-mass distributions in the western South Atlantic; A section from South Georgia Island (54S) northward across the equator. *Journal of Marine Research*, *52*(1), 55–81.

Walin, G. (1982). On the relation between sea-surface heat flow and thermal circulation in the ocean. *Tellus*, *34*(2), 187–195.

Warren, B. A. (1972). Insensitivity of subtropical mode water characteristics to meteorological fluctuations. *Deep Sea Research and Oceanographic Abstracts*, *19*(1), 1–19.

Worthington, L. V. (1959). The 18° water in the Sargasso Sea. *Deep Sea Research (1953)*, *5*(2), 297–305.

Worthington, L. V. (1972). Negative oceanic heat flux as a cause of water-mass formation. *Journal of Physical Oceanography*, *2*(3), 205–211.

Worthington, L. V. (1976). *On the North Atlantic circulation. johns hopkins oceanographic studies no. 6*. John Hopkins University Press. (110 pp)

Xu, L., Xie, S.-P., & Liu, Q. (2012). Mode water ventilation and subtropical countercurrent over the North Pacific in CMIP5 simulations and future projections. *Journal of Geophysical Research: Oceans*, *117*(C12).

Figure 2.

A
B
C
D
80
Latitude
Longitude
30°S
33°S
36°S
39°S
42°S
45°S
60°W
45°W
30°W
15°W
0°
15°E
50
100
150
200
250
300

Figure 1.

Mean Heat Flux
A.1
W/m^2
Heat flux - Apr - Jun
B.1
Heat flux - May - Jul
C.1
Heat flux - Jun - Aug
D.1
Mean Wind Speed
A.2
m/s
Wind speed - Apr - Jun
B.2
Wind speed - May - Jul
C.2
Wind speed - Jun - Aug
D.2
Mean E - P
A.3
mm/day
E - P - Apr - Jun
B.3
E - P - May - Jul
C.3
E - P - Jun - Aug
D.3
Latitude
Longitude
A.4
Volume
$\times 10^{14}$
Months
B.4
Years

Figure 7.

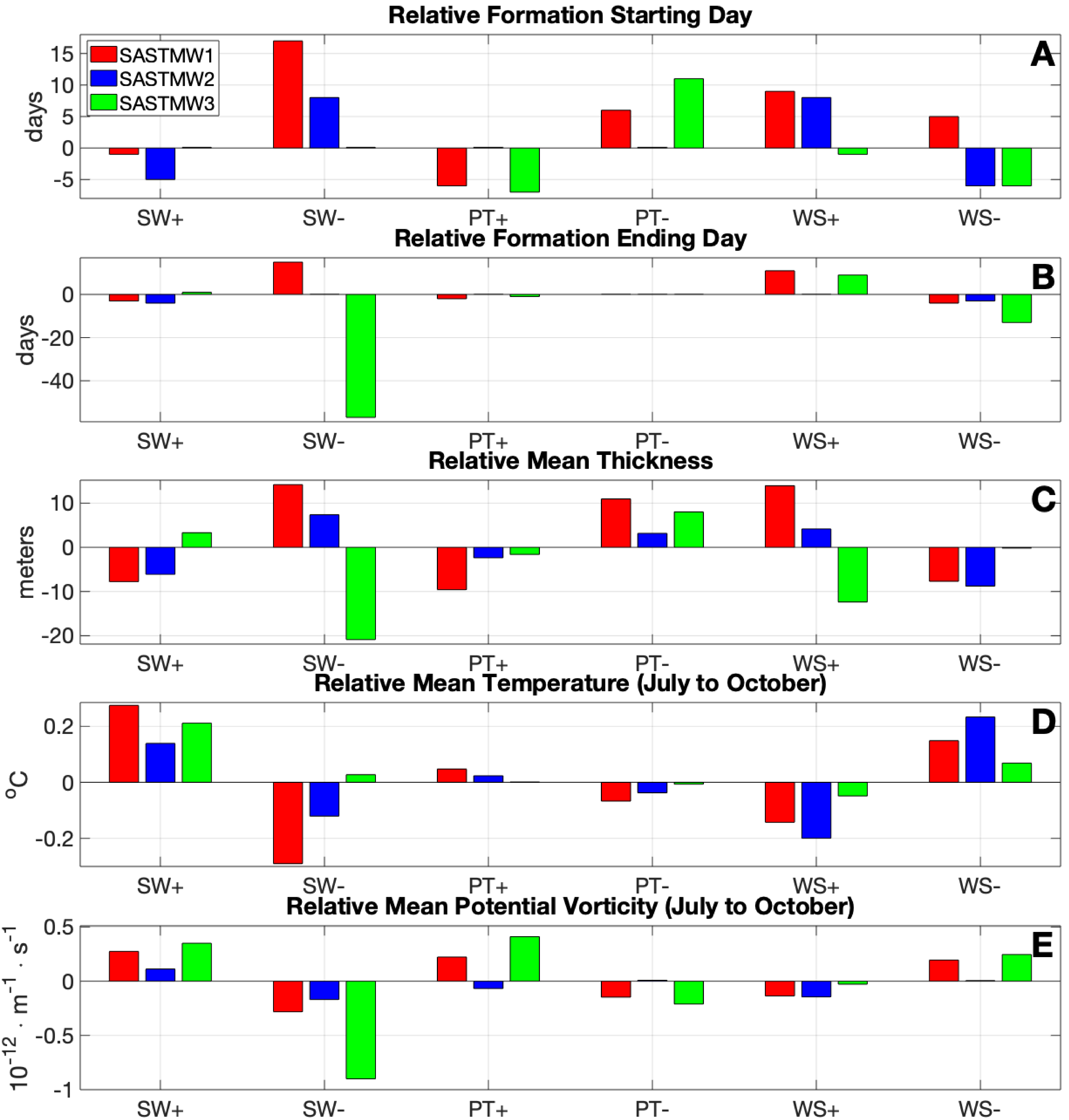
Relative Formation Starting Day
A
days
SASTMW1
SASTMW2
SASTMW3
15
10
5
0
-5
SW+
SW-
PT+
PT-
WS+
WS-
Relative Formation Ending Day
B
days
0
-20
-40
Relative Mean Thickness
C
meters
10
0
-10
-20
Relative Mean Temperature (July to October)
D
°C
0.2
0
-0.2
Relative Mean Potential Vorticity (July to October)
E
$10^{-12} \cdot m^{-1} \cdot s^{-1}$
0.5
0
-0.5
-1

Figure 8.


SW+
SASTMW1
SASTMW2
SASTMW3
SW-
PT+
PT-
WS+
WS-
Anomaly (%)
Volume
Area
Thickness
STMW Intensity
OHS
100
50
0
-50
-100
2
1
0
-1
-2

Figure 9.

A
B
C
D
Latitude
Longitude
24°S
30°S
36°S
42°S
48°S
54°W
36°W
18°W
0°
18°E
1
2
3
W · m^{-2}
mm · day^{-1}
m · s^{-2}
$\times 10^{-3}$
m · s^{-1}
220
200
180
160
140
120
100
80
4.5
4
3.5
3
2.5
2
1.5
1
0.5
5
0
-5
-10
-15
11
10
9
8
7
6
5
4
3

Figure 6.

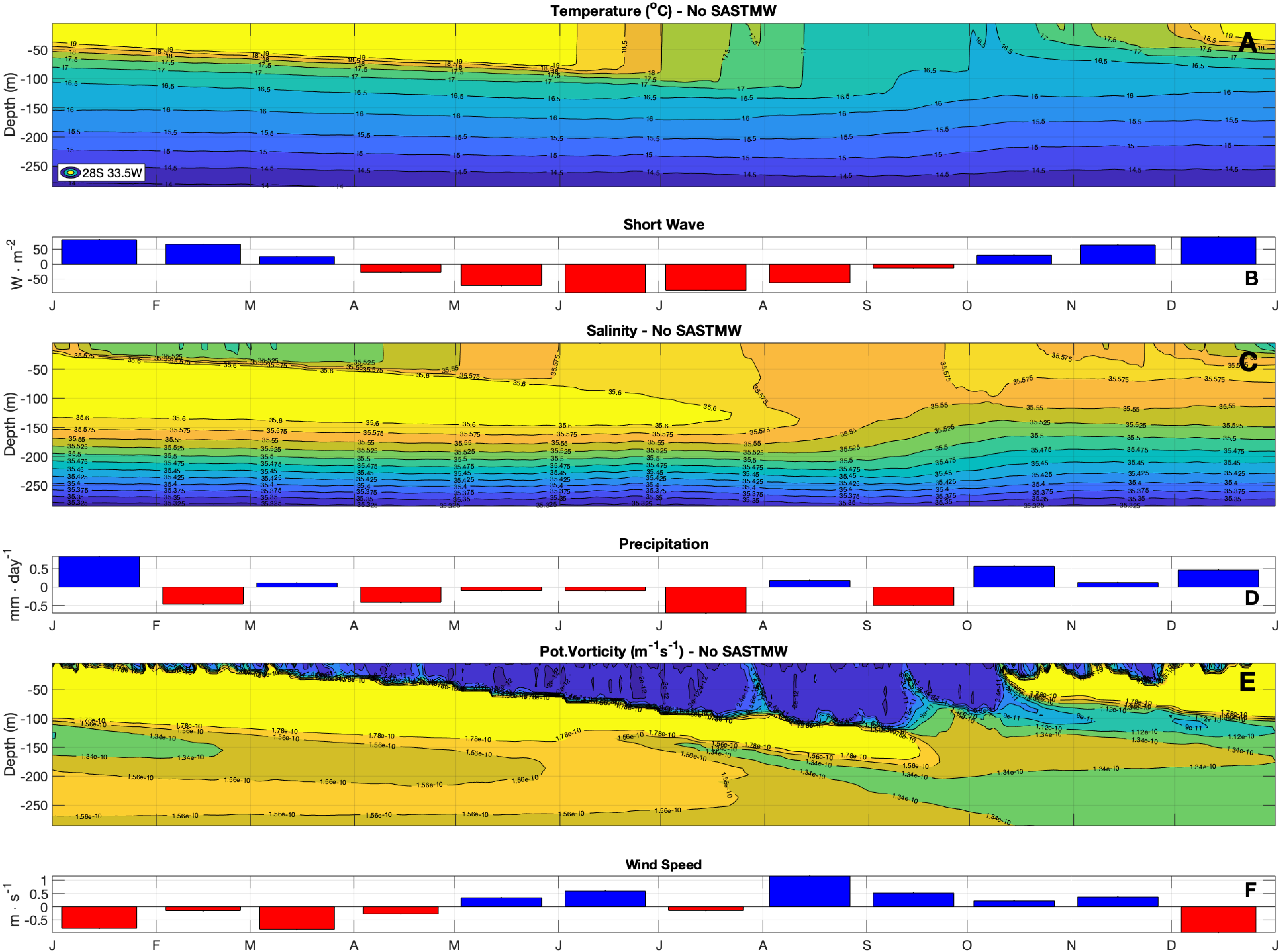
Temperature (^{o}C) - No SASTMW
Depth (m)
28S 33.5W
A
Short Wave
W · m^{-2}
B
J F M A M J J A S O N D J
Salinity - No SASTMW
Depth (m)
C
Precipitation
mm · day^{-1}
D
J F M A M J J A S O N D J
Pot.Vorticity (m^{-1}s^{-1}) - No SASTMW
Depth (m)
E
Wind Speed
m · s^{-1}
F
J F M A M J J A S O N D J

Figure 3.

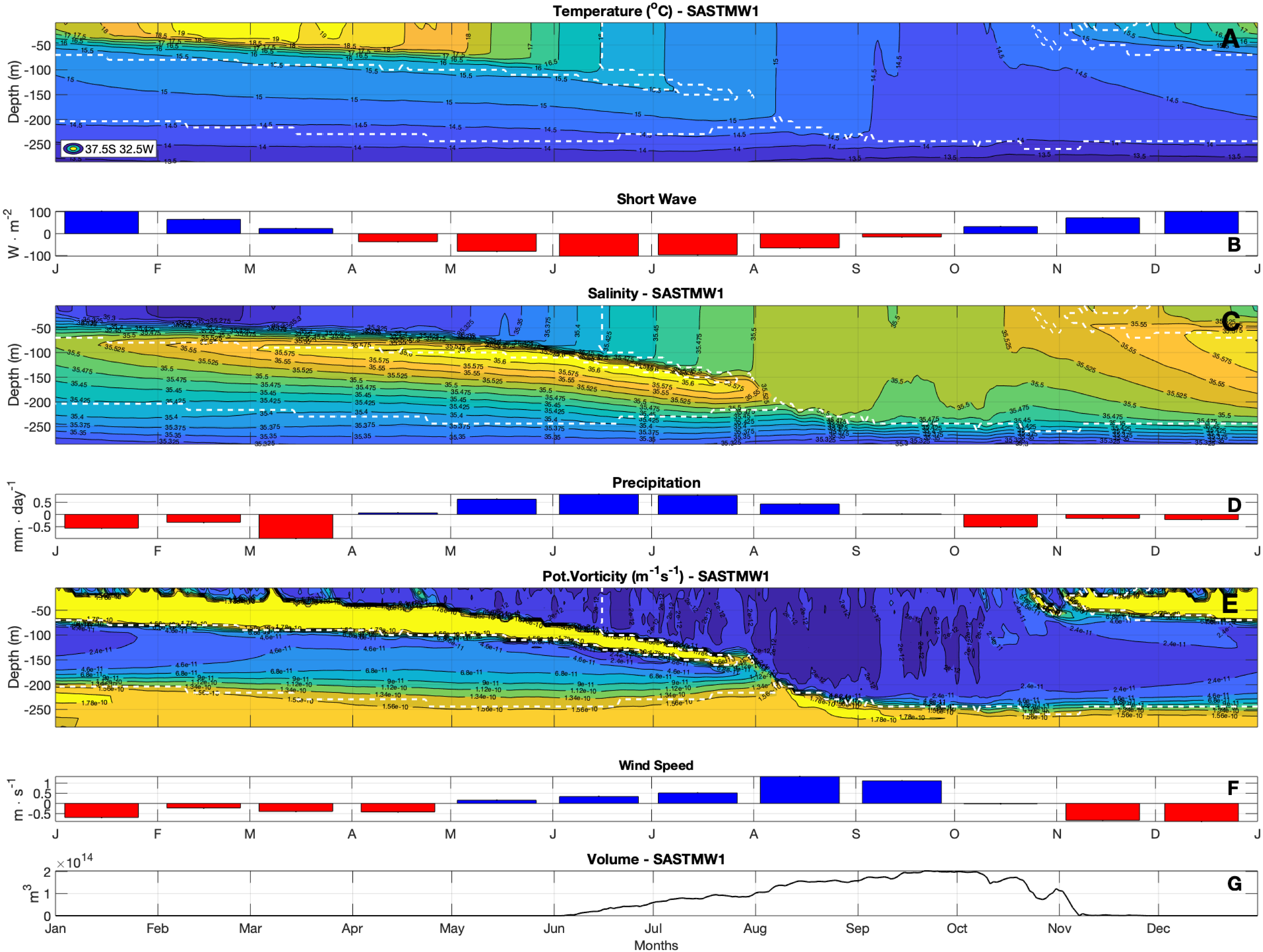

Temperature (°C) - SASTMW1
37.5S 32.5W
Depth (m)
A
Short Wave
W · m⁻²
B
Salinity - SASTMW1
C
Precipitation
mm · day⁻¹
D
Pot.Vorticity (m⁻¹s⁻¹) - SASTMW1
E
Wind Speed
m · s⁻¹
F
Volume - SASTMW1
×10¹⁴
m³
G
Jan
Feb
Mar
Apr
May
Jun
Jul
Aug
Sep
Oct
Nov
Dec
Months

Figure 4.

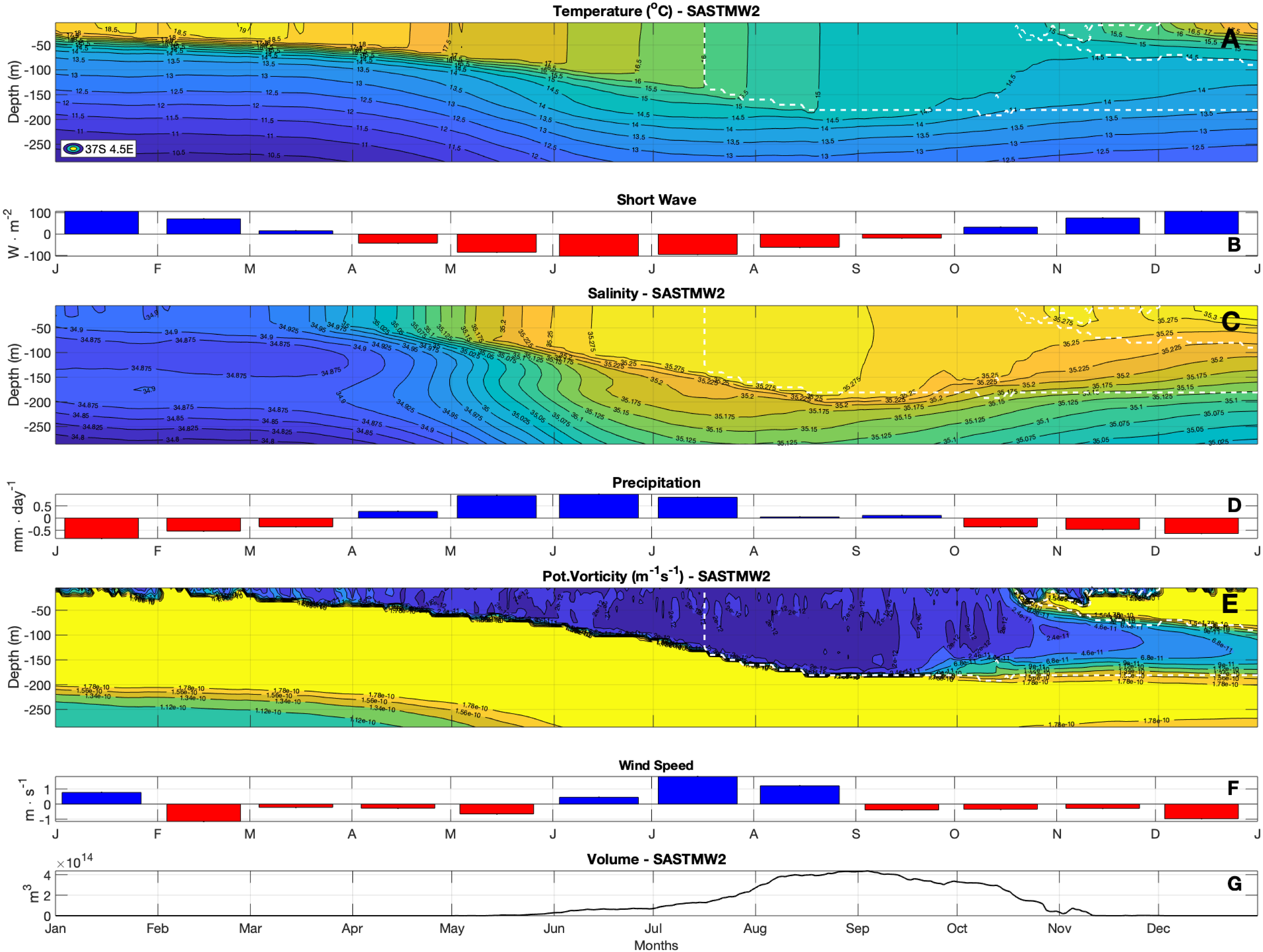

Temperature (°C) - SASTMW2
A
Depth (m)
37S 4.5E
Short Wave
B
W · m^-2
Salinity - SASTMW2
C
Depth (m)
Precipitation
D
mm · day^-1
Pot.Vorticity (m^-1 s^-1) - SASTMW2
E
Depth (m)
Wind Speed
F
m · s^-1
Volume - SASTMW2
G
m^3
×10^14
Jan
Feb
Mar
Apr
May
Jun
Jul
Aug
Sep
Oct
Nov
Dec
Months

Figure 5.

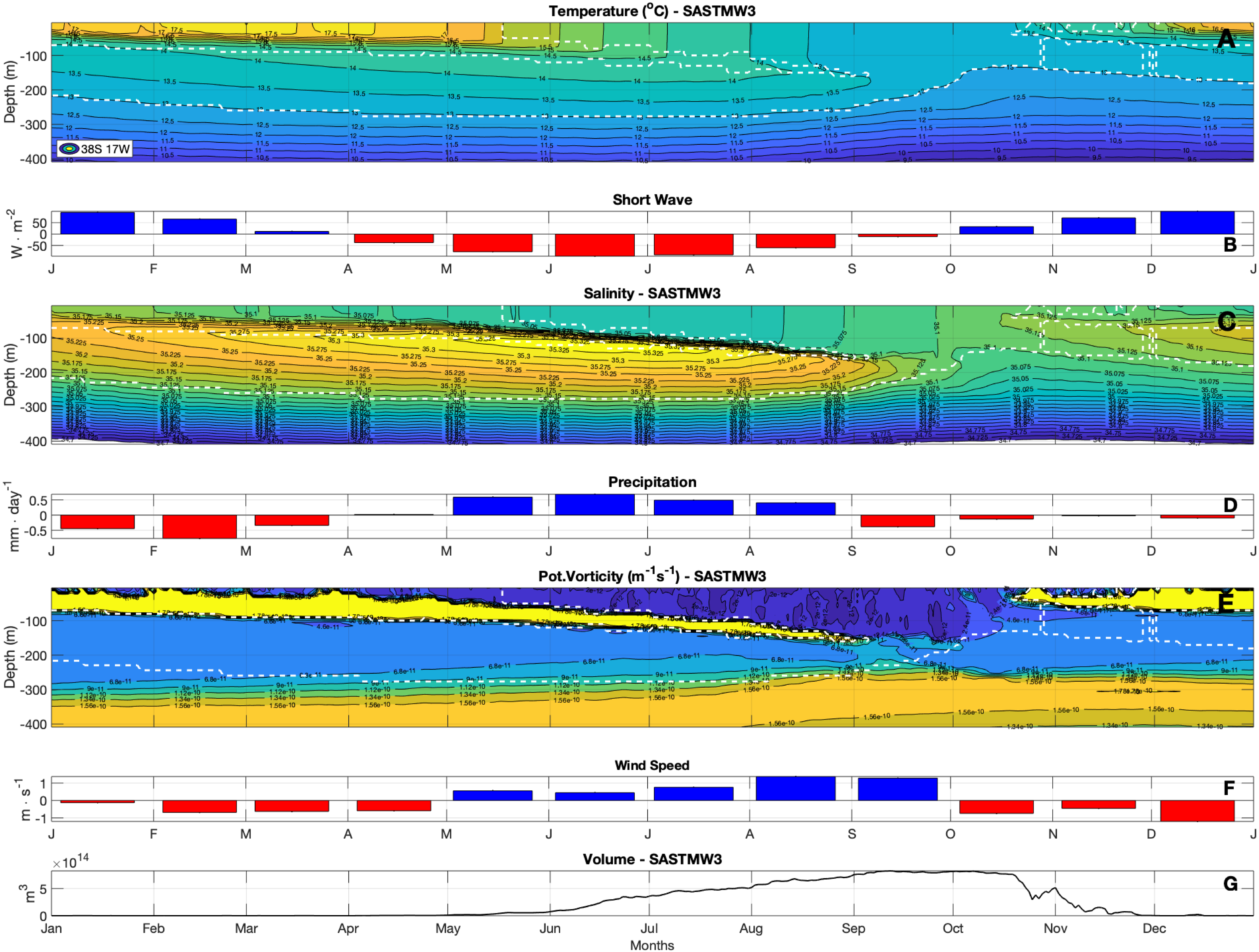

Temperature (°C) - SASTMW3
A
Depth (m)
-100
-200
-300
-400
38S 17W
Short Wave
B
W · m⁻²
50
0
-50
J F M A M J J A S O N D J
Salinity - SASTMW3
C
Depth (m)
Precipitation
D
mm · day⁻¹
0.5
0
-0.5
Pot.Vorticity (m⁻¹s⁻¹) - SASTMW3
E
Depth (m)
Wind Speed
F
m · s⁻¹
1
0
-1
Volume - SASTMW3
G
×10¹⁴
m³
5
0
Jan Feb Mar Apr May Jun Jul Aug Sep Oct Nov Dec
Months

Supporting Information for "Simulated response of South Atlantic Subtropical Mode Water to air-sea processes"

Piero S. Bernardo[1], Olga T. Sato[1]and Andréa S. Taschetto[2]

[1]Oceanographic Institute of the University of São Paulo, São Paulo, Brazil

[2]Climate Change Research Centre, University of New South Wales, Sydney, New South Wales, Australia

Contents of this file

Introduction

The supporting information presented here in this document refers to the extra details of the model configuration used to identify the South Atlantic Subtropical Mode Water (Text 1) and the volume identified throughout the model's time series (Figure S4). We also present the tests of the possible criteria used for this identification (Text S2), the table of the tested criteria (Table S1) and the result of these variations on the observed volume (Figure S3).

The configuration of the developed sensitivity experiments and the basis for changing the short wave flux for the experiments were presented in two figures (Figure S1 and S2).

The results of the experiments by type of SASTMW are shown between Figure S5 and S22.

Finally, the calculation of the subtropical modal water intensity (STMW) was presented (Text S3). This is a important parameter used for the evaluation of the experiments.

Text S1.

The Community Earth System Model version 1.2.2 create simulations using up to seven geophysical models: atmosphere, sea-ice, land, river-runoff, ocean, land-ice and ocean-wave. These systems presents different versions: "active" (geophysical model), "data", "dead" (invalid information) or "stub" (interface data) and the information are transmitted from one system to another through a coupler that also synchronizes the step of the models for the same time (Vertenstein et al., 2013).

Text S2.

The identification sensitivity test of the South Atlantic Subtropical Mode Water (SASTMW) was developed to identify which criteria were more or less restrictive for this process. The important variables for the selection of SASTMW are: temperature, salinity, potential density, potential vorticity and vertical temperature gradient.

Therefore 14 variations of the criteria used by Bernardo and Sato (2020) were created (Table S1). The limits of the criteria for the aforementioned variables have been enlarged or reduced and the result on the volume of SASTMW observed on the surface and subsurface can be seen in the Figure S3. The volume referring to the application of criterion N^{o}.0 (Table S1) was subtracted from each time series of the volume of the different cases.

Text S3.

The STMW intensity (I) is defined by the vertical integral of the potential vorticity (PV) anomaly (Qiu et al., 2006). The anomaly is calculated using a reference PV value (Q_a) relative to the threshold 1.5×10^{-10} m^{-1} s^{-1}, used in the identification of the SASTMW. The equation of the STMW intensity is:

$$I = \int_{z_2}^{z_1} [Q_a - Q(z)]\, dz, \tag{1}$$

where z_1 is the depth of the 16°C isotherm, z_2 is the depth of the 13°C isotherm and $Q(z)$ is the PV value of each vertical layer.

References

Bernardo, P. S., & Sato, O. T. (2020). Volumetric Characterization of the South Atlantic Subtropical Mode Water Types. *Geophysical Research Letters*, *47*(8), e2019GL086653.

Qiu, B., Hacker, P., Chen, S., Donohue, K. A., Watts, D. R., Mitsudera, H., … Jayne, S. R. (2006). Observations of the subtropical mode water evolution from the Kuroshio Extension System Study. *Journal of Physical Oceanography*, *36*(3), 457–473.

Vertenstein, M., Bertini, A., Craig, T., Edwards, J., Levy, M., Mai, A., & Schollenberger, J. (2013). CESM user's guide (CESM1. 2 release series user's guide). *NCAR Tech. Note*.

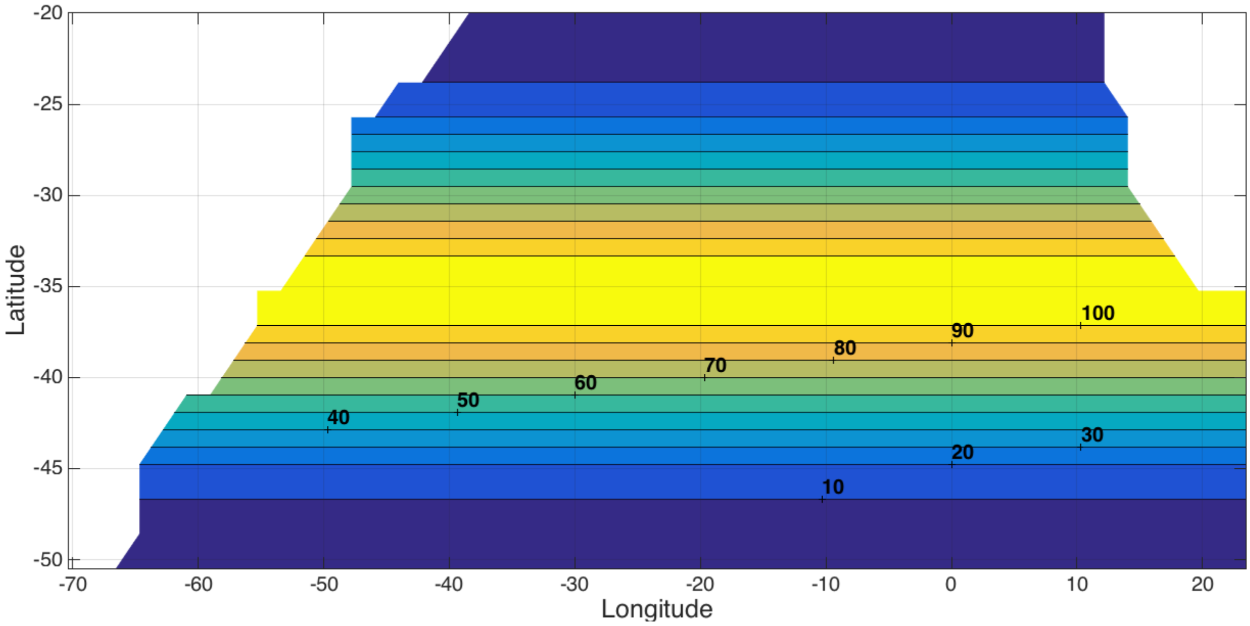

Figure S1. Scheme used to create the SASTMW formation sensitivity experiments over a year using the CESM model. The central band (100) represents the total application of the changes created in each experiment scenario. All the number (from 100 to 10) represent the percentage of the change applied per area.

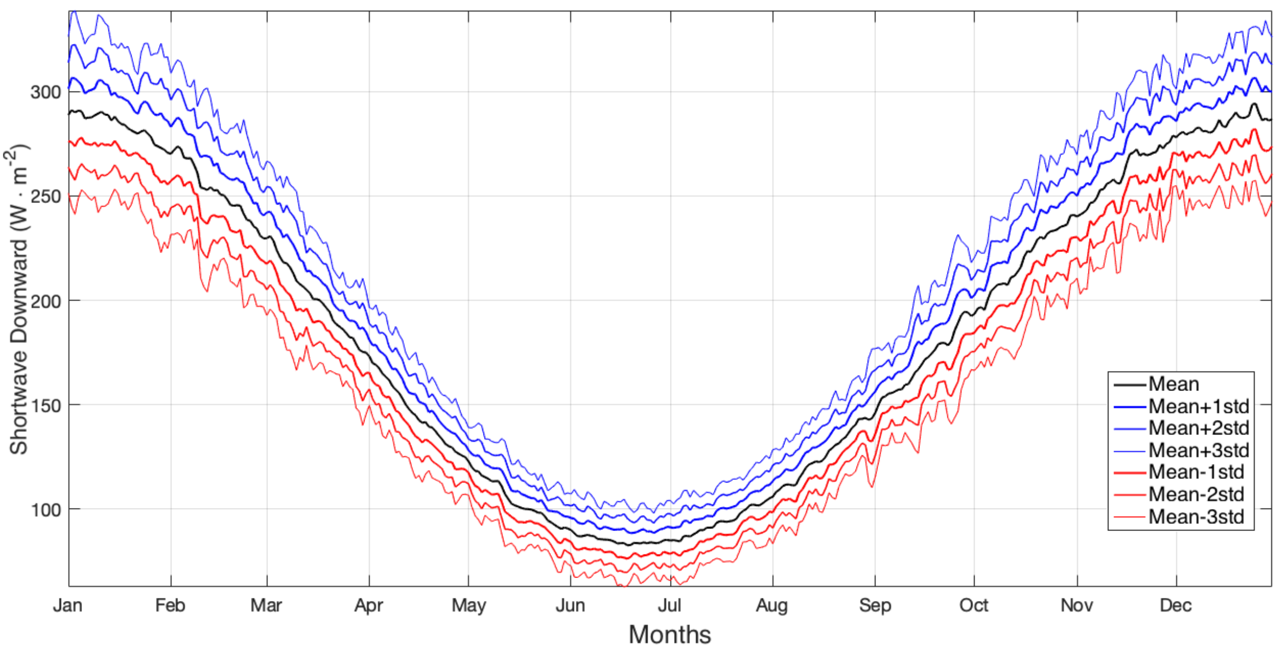

Figure S2. Climatological time series of the shortwave downward flux component mean and mean plus/minus n times the standard deviation for the period of 1971 to 2009, region of 25°S to 45°S, 60°W to 20°E.

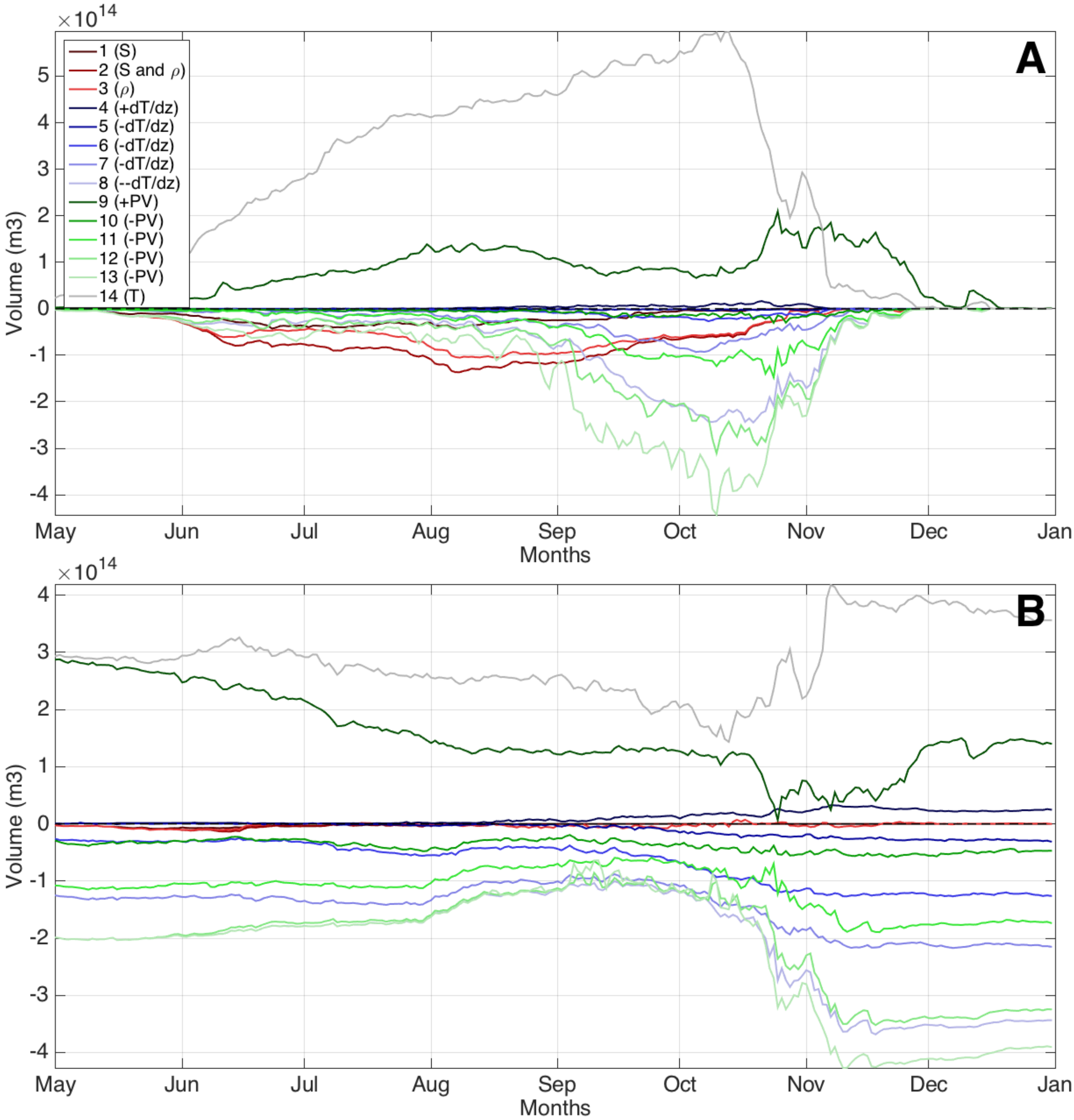

Figure S3. Comparison between the difference of the volume resulting from the use of different criteria for the identification of SASTMW, in relation to the criterion determined by Bernardo and Sato (2020) and applied in the article (No.0 in Table S1). The values for each criterion are specified in Table S1. Diagram A: Surface; B: Subsurface.

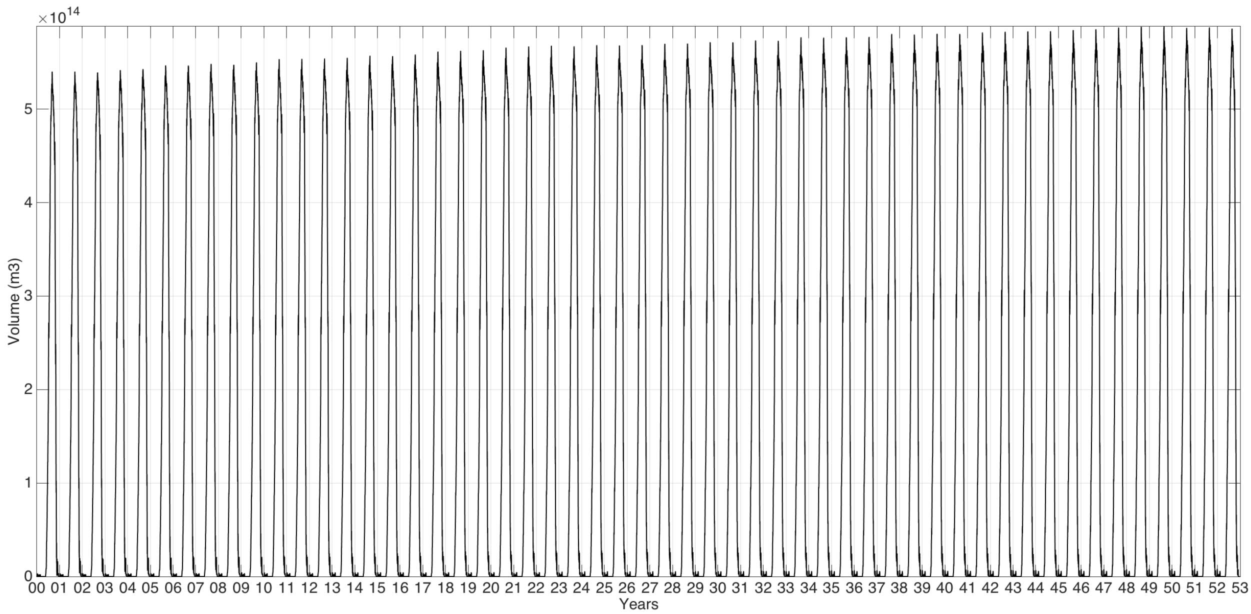

Figure S4. Times series of volume of the SASTMW in the surface of the 52-years CESM - Normal Year Forcing control run.

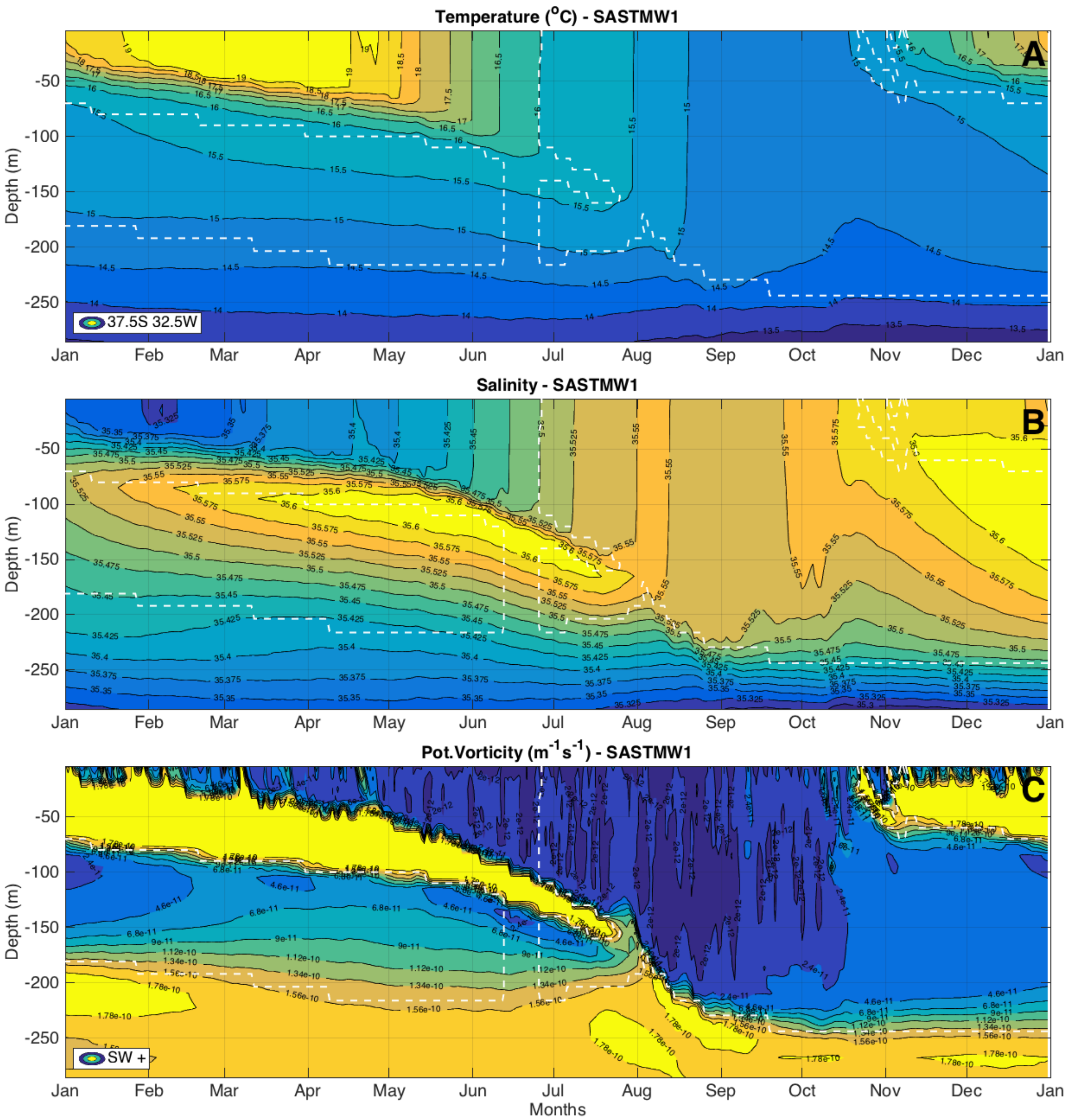

Figure S5. Temperature, shortwave radiation, salinity, precipitation, potential vorticity, and wind speed variation over one year at 37.5°S, 32.5°W in the CESM SW+ experiment. The white contour represents the SASTMW 1 identified throughout the cycle. All the PV values greater than 1.5×10^{-10} m^{-1} s^{-1} were included in the maximum value contour.

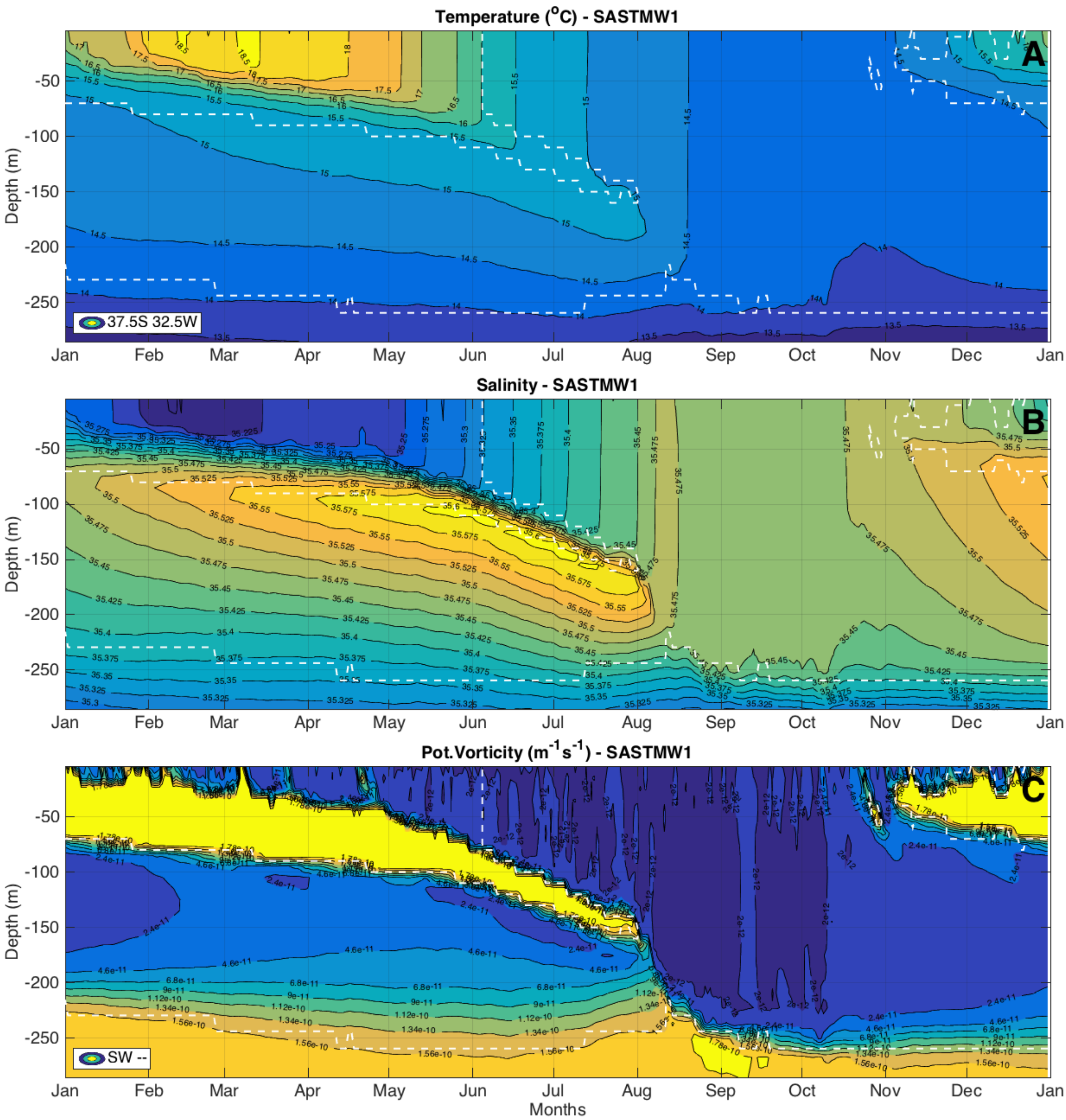

Figure S6. Temperature, shortwave radiation, salinity, precipitation, potential vorticity, and wind speed variation over one year at 37.5°S, 32.5°W in the CESM SW- experiment. The white contour represents the SASTMW 1 identified throughout the cycle. All the PV values greater than 1.5×10^{-10} m^{-1} s^{-1} were included in the maximum value contour.

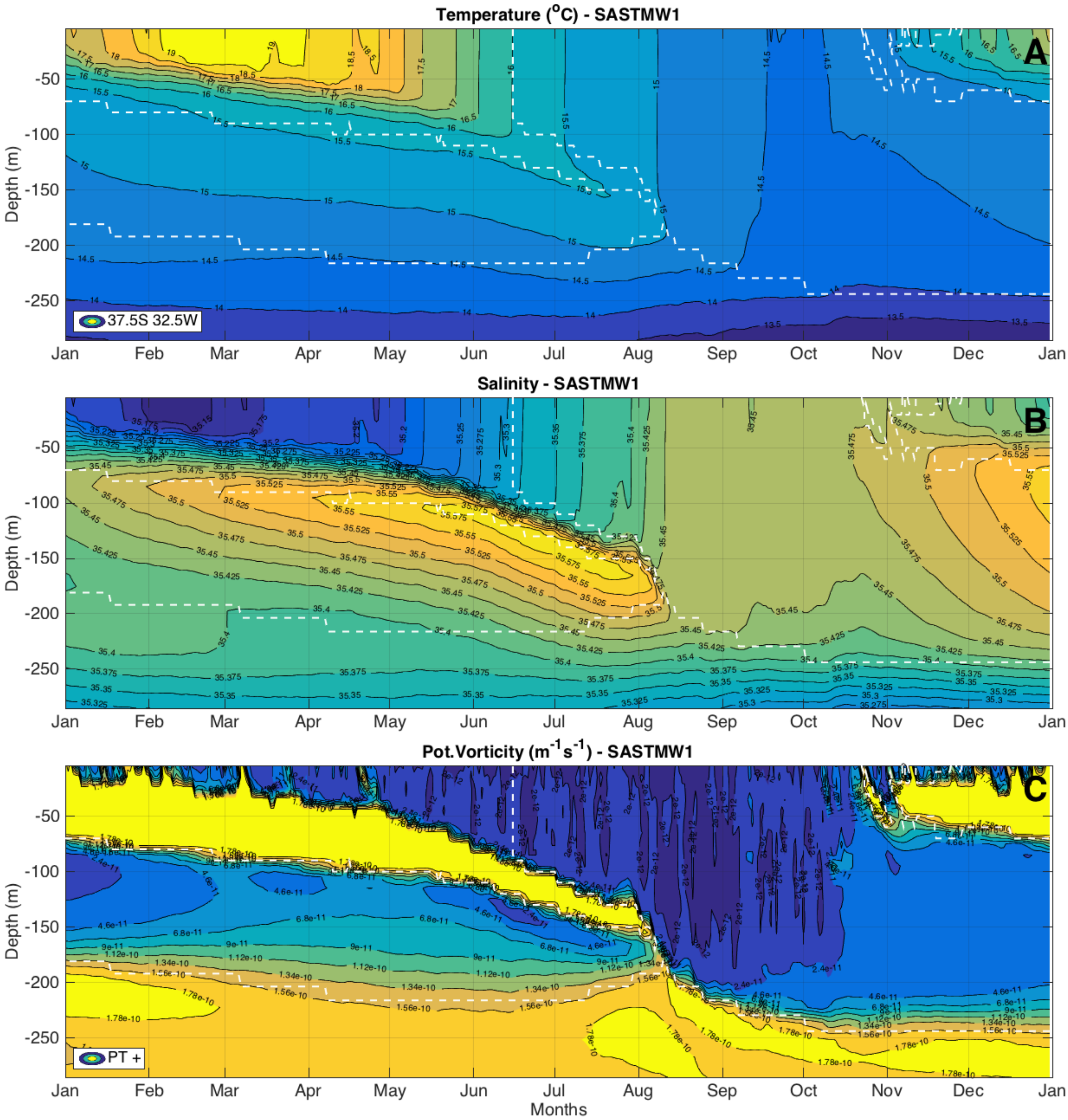

Figure S7. Temperature, shortwave radiation, salinity, precipitation, potential vorticity, and wind speed variation over one year at 37.5°S, 32.5°W in the CESM PT+ experiment. The white contour represents the SASTMW 1 identified throughout the cycle. All the PV values greater than 1.5×10^{-10} m^{-1} s^{-1} were included in the maximum value contour.

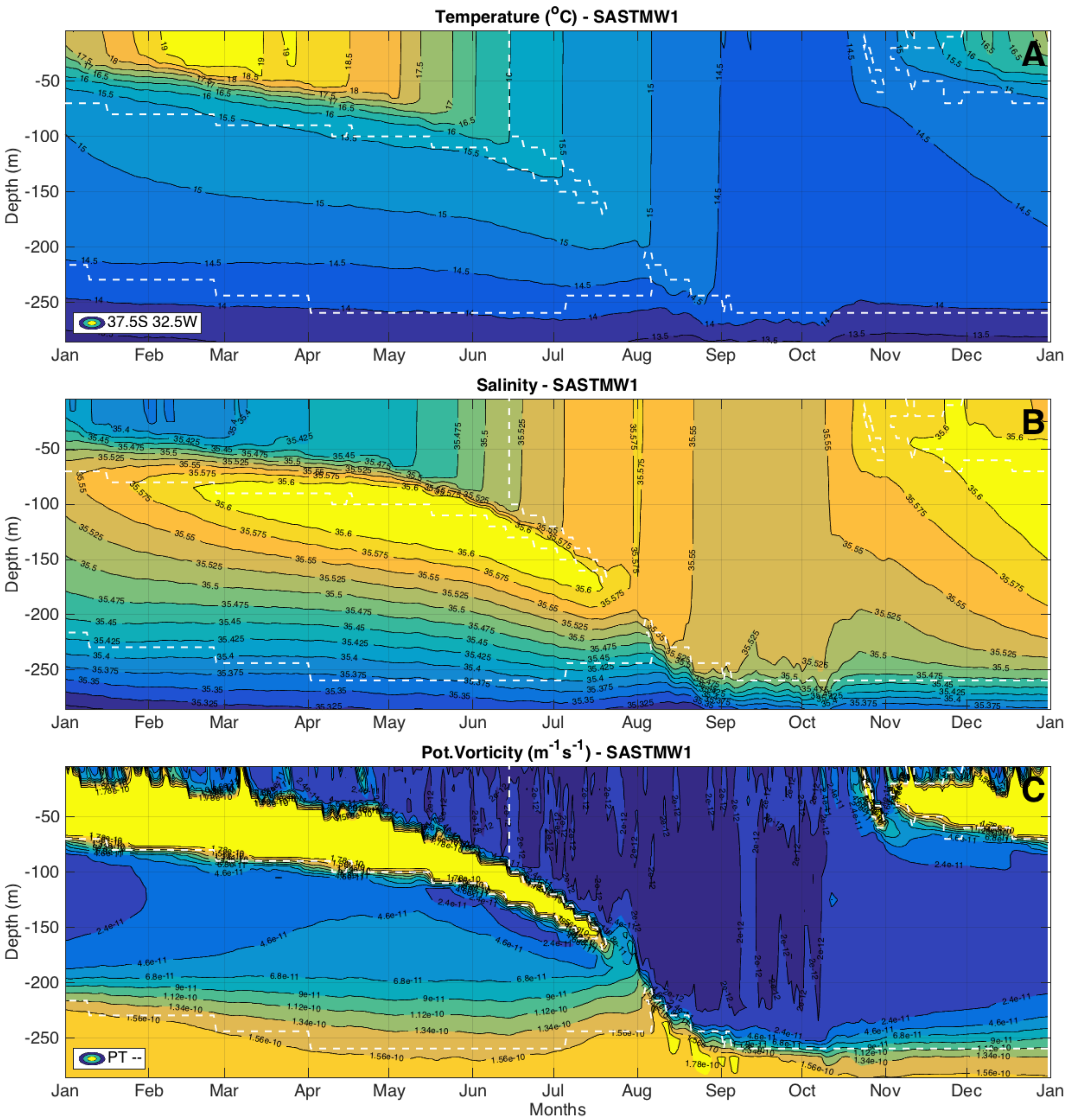

Figure S8. Temperature, shortwave radiation, salinity, precipitation, potential vorticity, and wind speed variation over one year at 37.5°S, 32.5°W in the CESM PT- experiment. The white contour represents the SASTMW 1 identified throughout the cycle. All the PV values greater than 1.5×10^{-10} m^{-1} s^{-1} were included in the maximum value contour.

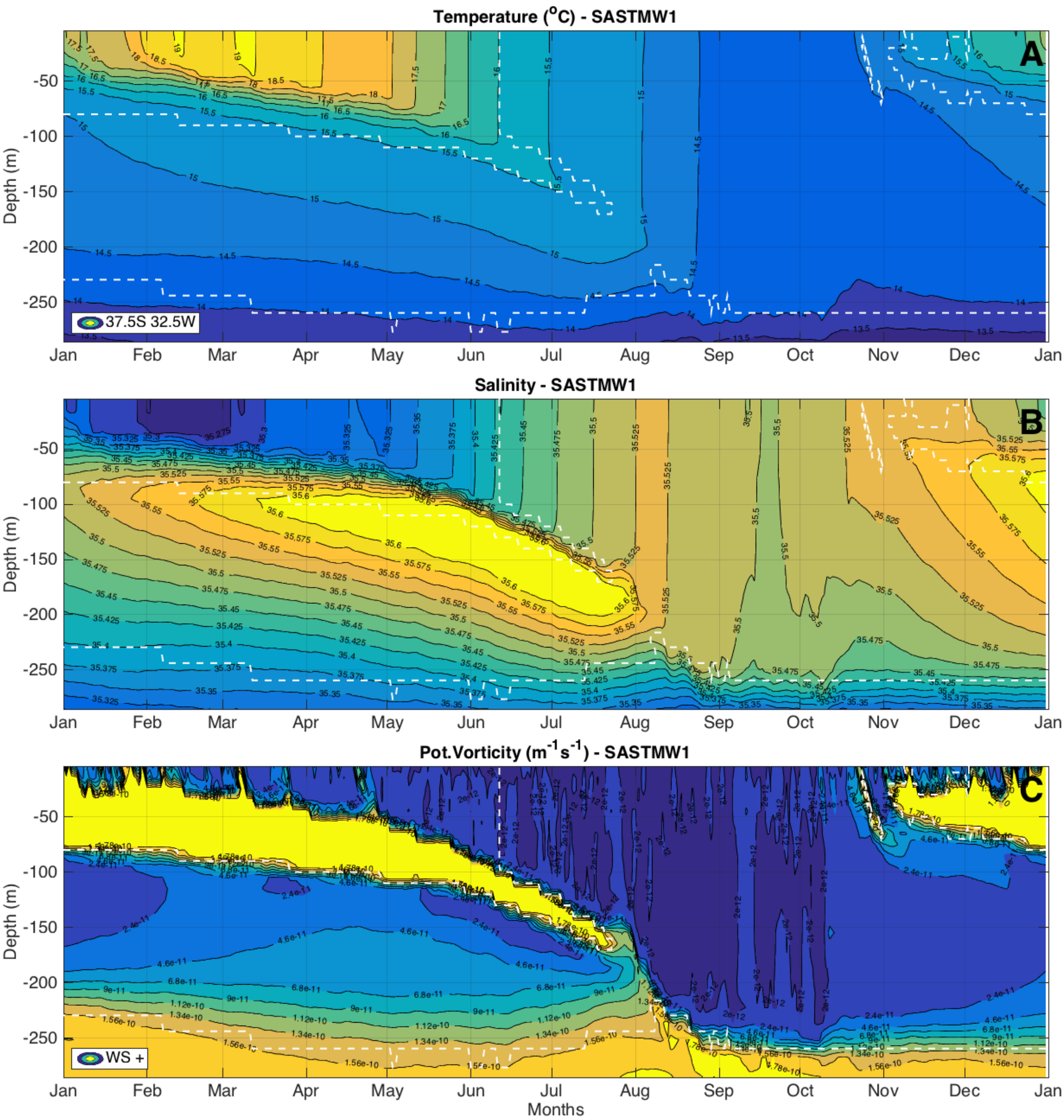

Figure S9. Temperature, shortwave radiation, salinity, precipitation, potential vorticity, and wind speed variation over one year at 37.5°S, 32.5°W in the CESM WS+ experiment. The white contour represents the SASTMW 1 identified throughout the cycle. All the PV values greater than 1.5×10^{-10} m^{-1} s^{-1} were included in the maximum value contour.

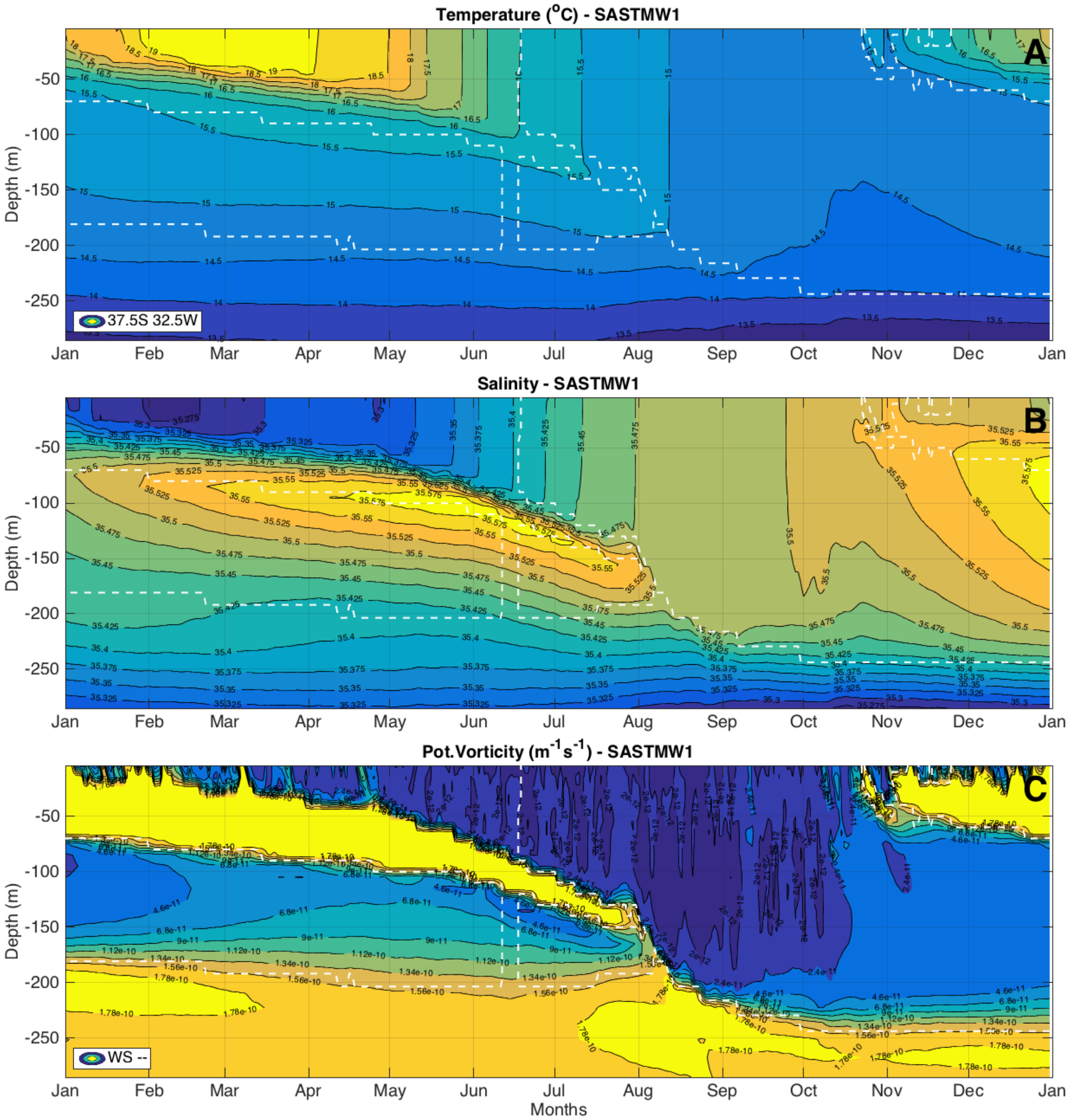

Figure S10. Temperature, shortwave radiation, salinity, precipitation, potential vorticity, and wind speed variation over one year at 37.5°S, 32.5°W in the CESM WS- experiment. The white contour represents the SASTMW 1 identified throughout the cycle. All the PV values greater than 1.5×10^{-10} m^{-1} s^{-1} were included in the maximum value contour.

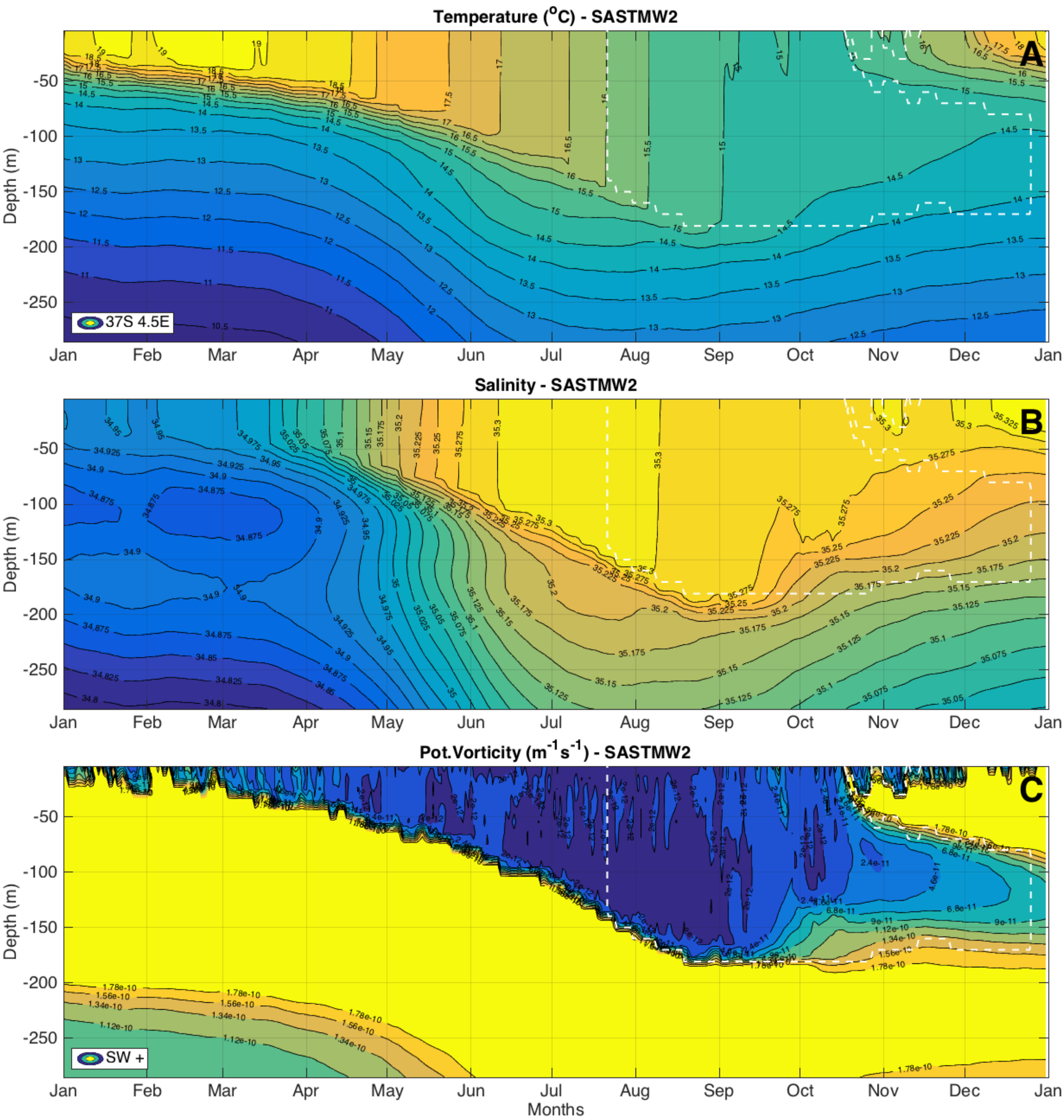

Figure S11. Temperature, shortwave radiation, salinity, precipitation, potential vorticity, and wind speed variation over one year at 37°S, 4.5°E in the CESM SW+ experiment. The white contour represents the SASTMW 2 identified throughout the cycle. All the PV values greater than 1.5×10^{-10} m^{-1} s^{-1} were included in the maximum value contour.

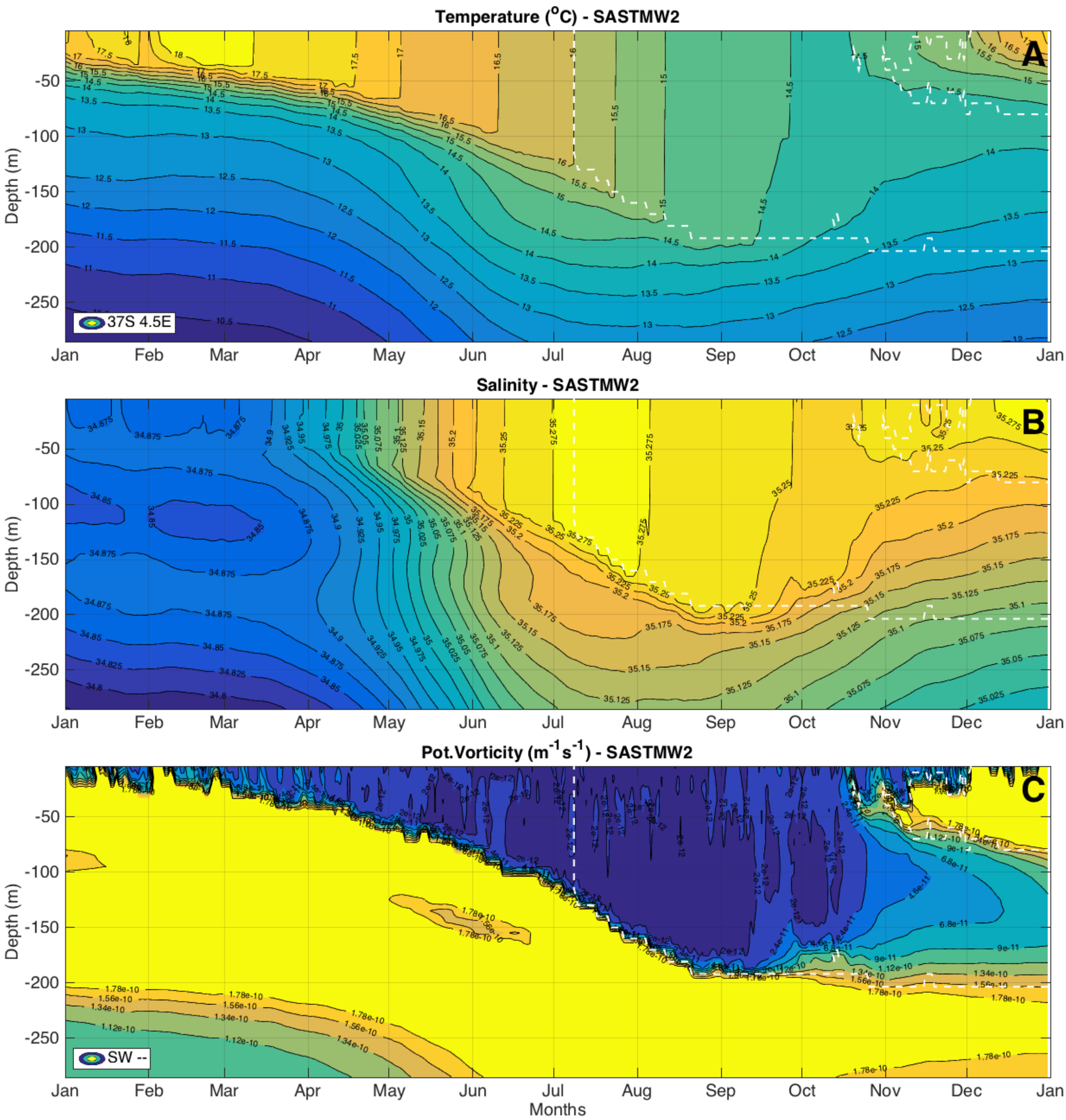

Figure S12. Temperature, shortwave radiation, salinity, precipitation, potential vorticity, and wind speed variation over one year at 37°S, 4.5°E in the CESM SW- experiment. The white contour represents the SASTMW 2 identified throughout the cycle. All the PV values greater than 1.5×10^{-10} m^{-1} s^{-1} were included in the maximum value contour.

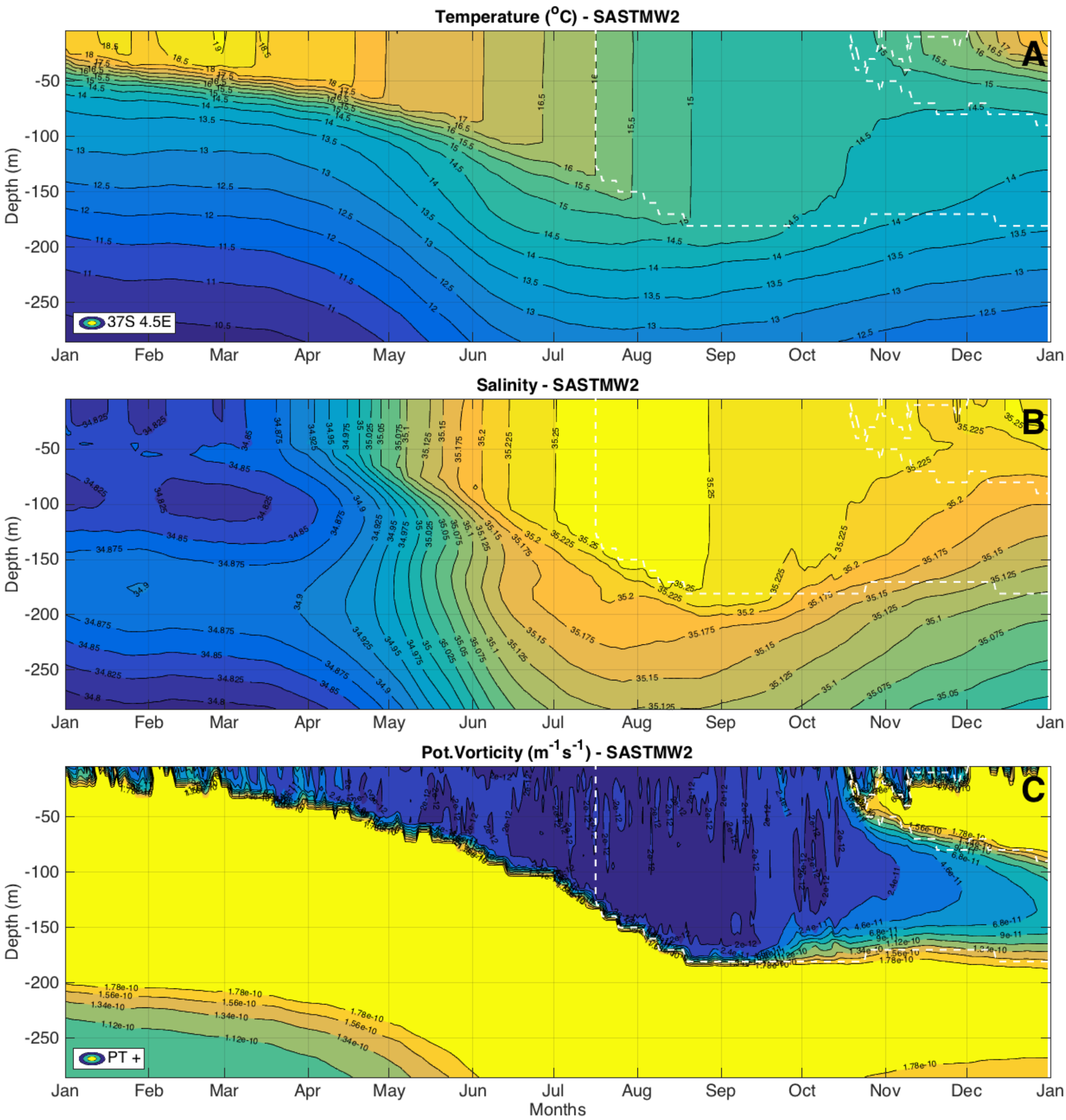

Figure S13. Temperature, shortwave radiation, salinity, precipitation, potential vorticity, and wind speed variation over one year at 37°S, 4.5°E in the CESM PT+ experiment. The white contour represents the SASTMW 2 identified throughout the cycle. All the PV values greater than 1.5×10^{-10} m^{-1} s^{-1} were included in the maximum value contour.

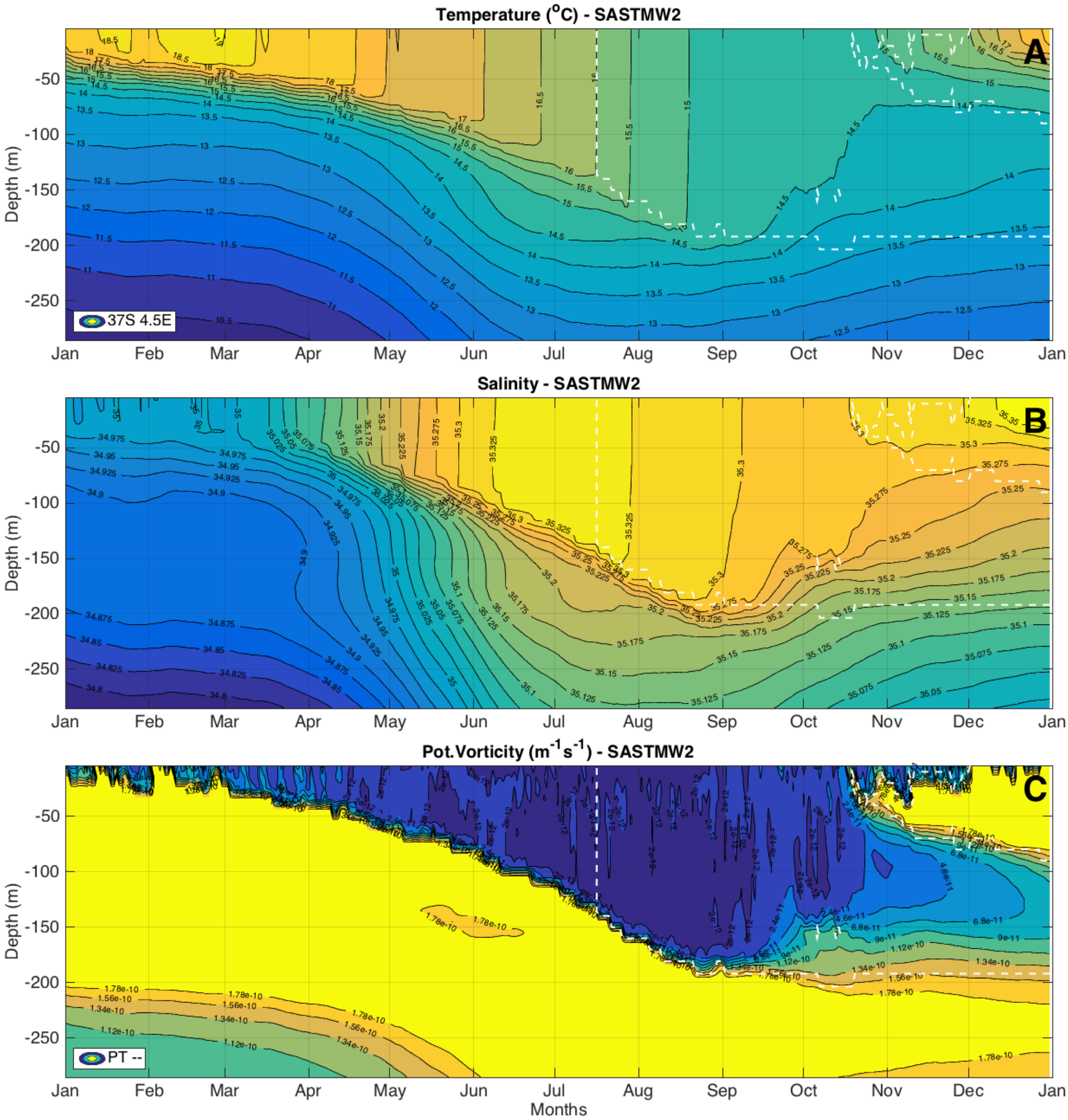

Figure S14. Temperature, shortwave radiation, salinity, precipitation, potential vorticity, and wind speed variation over one year at 37°S, 4.5°E in the CESM PT- experiment. The white contour represents the SASTMW 2 identified throughout the cycle. All the PV values greater than 1.5×10^{-10} m^{-1} s^{-1} were included in the maximum value contour.

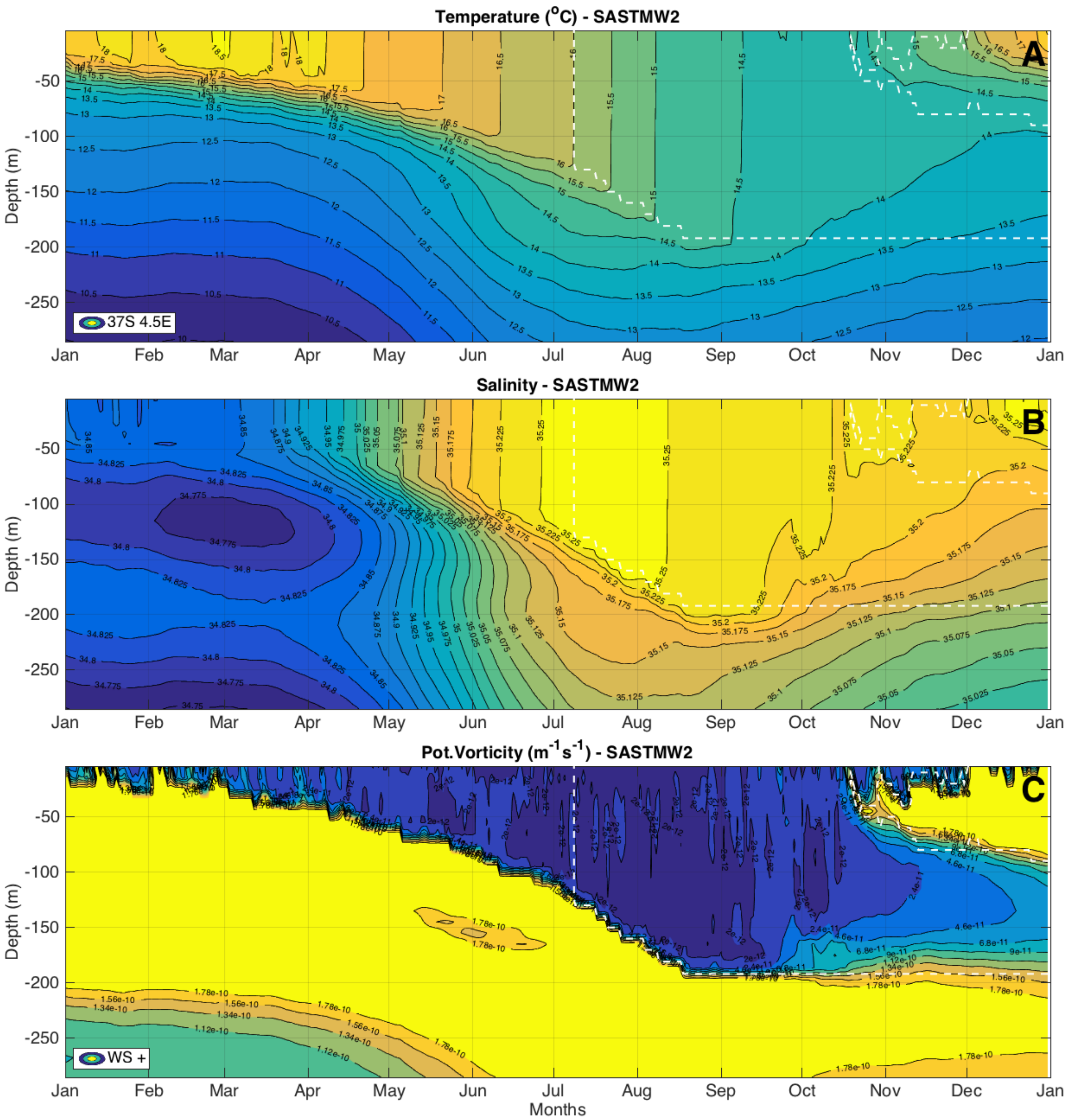

Figure S15. Temperature, shortwave radiation, salinity, precipitation, potential vorticity, and wind speed variation over one year at 37°S, 4.5°E in the CESM WS+ experiment. The white contour represents the SASTMW 2 identified throughout the cycle. All the PV values greater than 1.5×10^{-10} m^{-1} s^{-1} were included in the maximum value contour.

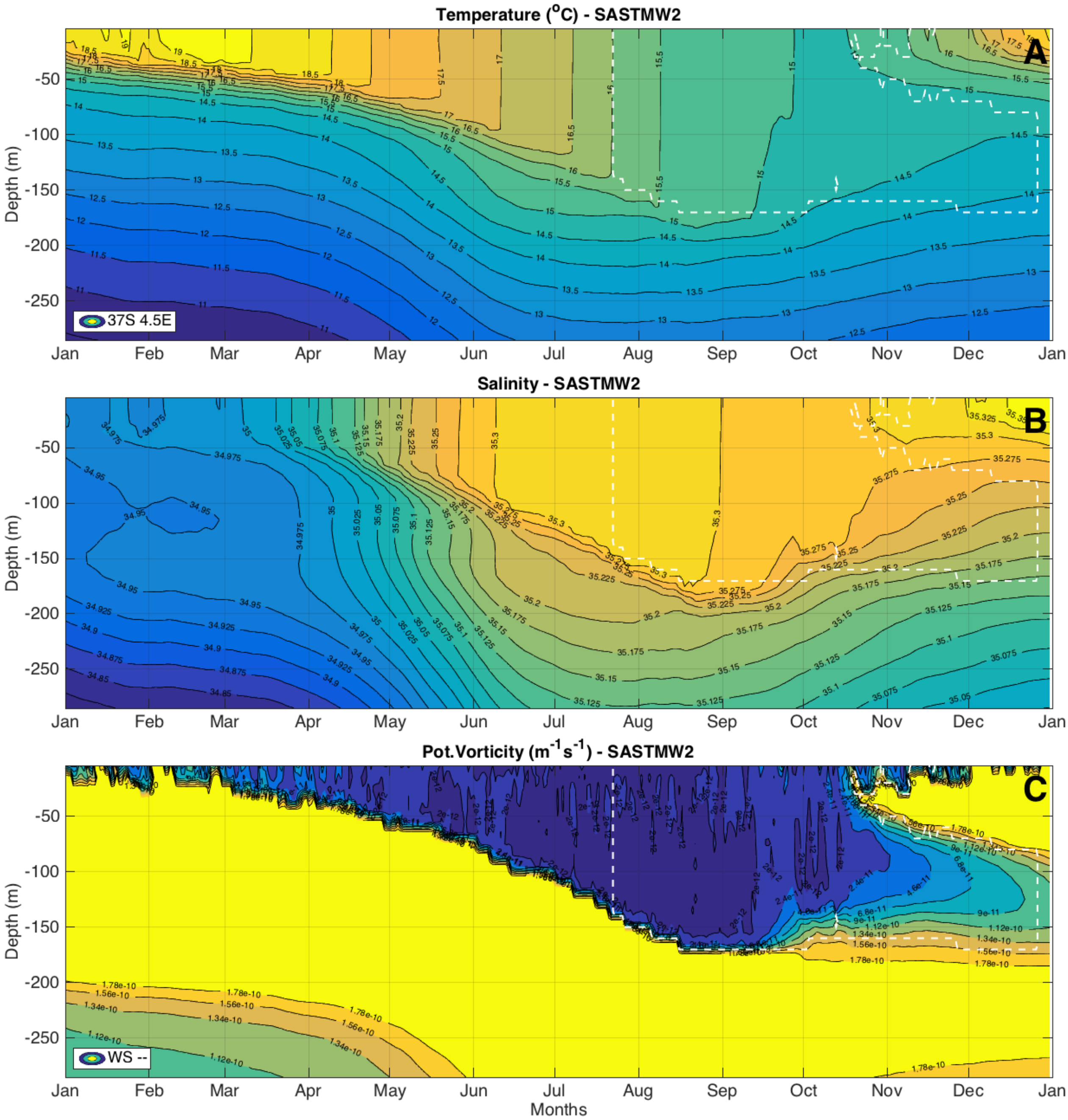

Figure S16. Temperature, shortwave radiation, salinity, precipitation, potential vorticity, and wind speed variation over one year at 37°S, 4.5°E in the CESM WS- experiment. The white contour represents the SASTMW 2 identified throughout the cycle. All the PV values greater than 1.5×10^{-10} m^{-1} s^{-1} were included in the maximum value contour.

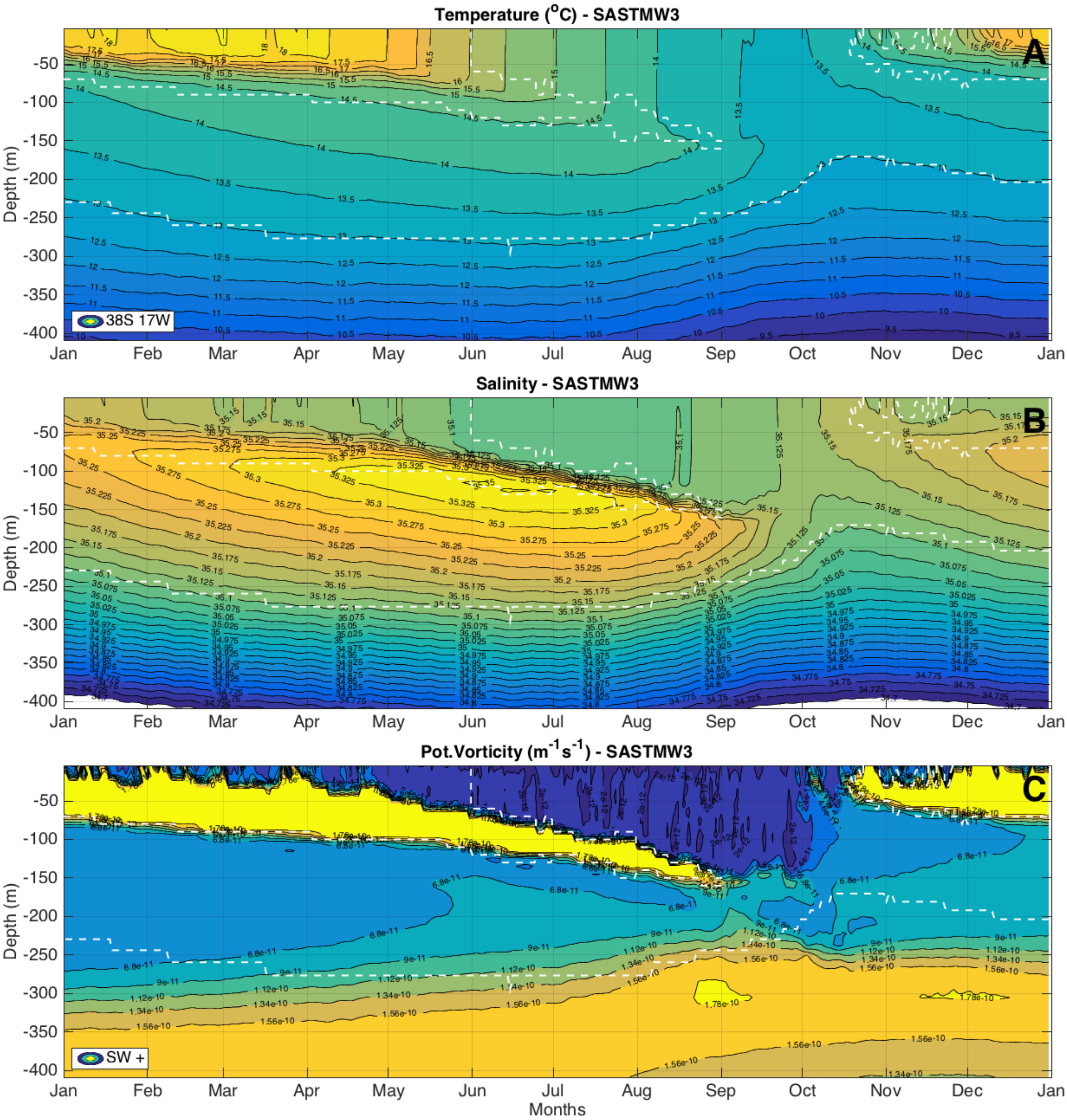

Figure S17. Temperature, shortwave radiation, salinity, precipitation, potential vorticity, and wind speed variation over one year at 38°S, 17°W in the CESM SW+ experiment. The white contour represents the SASTMW 3 identified throughout the cycle. All the PV values greater than 1.5×10^{-10} m^{-1} s^{-1} were included in the maximum value contour.

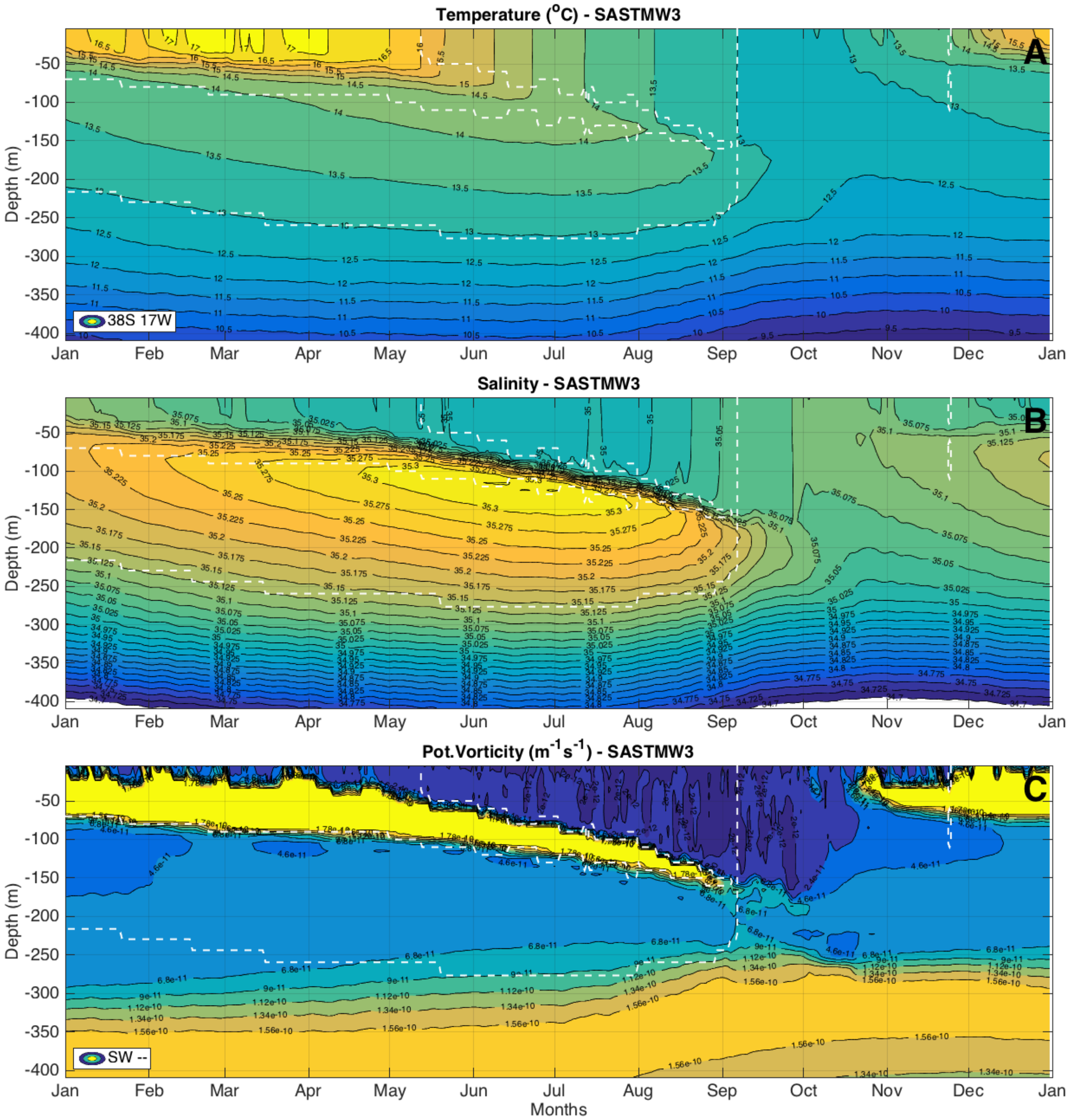

Figure S18. Temperature, shortwave radiation, salinity, precipitation, potential vorticity, and wind speed variation over one year at 38°S, 17°W in the CESM SW- experiment. The white contour represents the SASTMW 3 identified throughout the cycle. All the PV values greater than 1.5×10^{-10} m^{-1} s^{-1} were included in the maximum value contour.

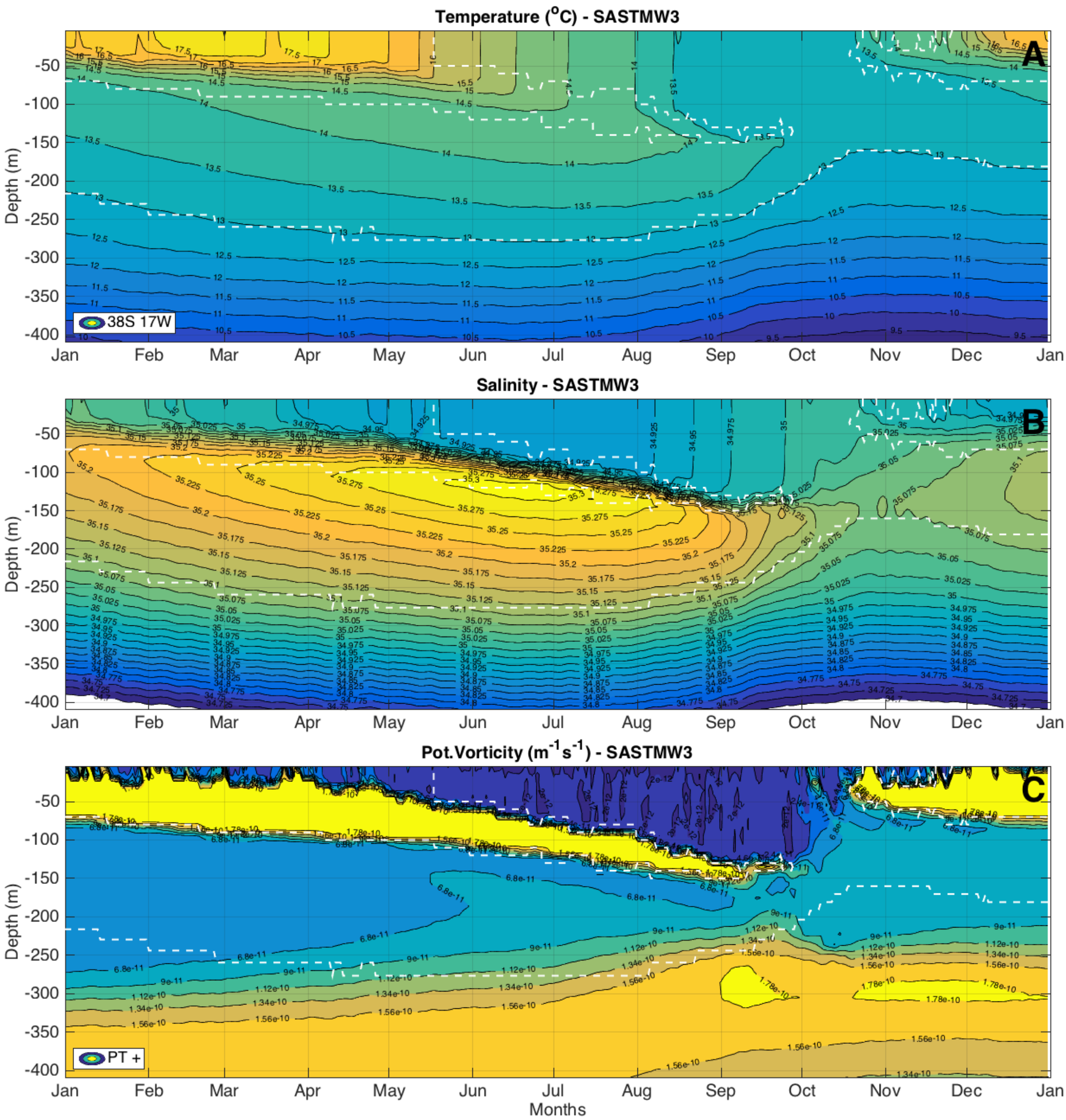

Figure S19. Temperature, shortwave radiation, salinity, precipitation, potential vorticity, and wind speed variation over one year at 38°S, 17°W in the CESM PT+ experiment. The white contour represents the SASTMW 3 identified throughout the cycle. All the PV values greater than 1.5×10^{-10} m^{-1} s^{-1} were included in the maximum value contour.

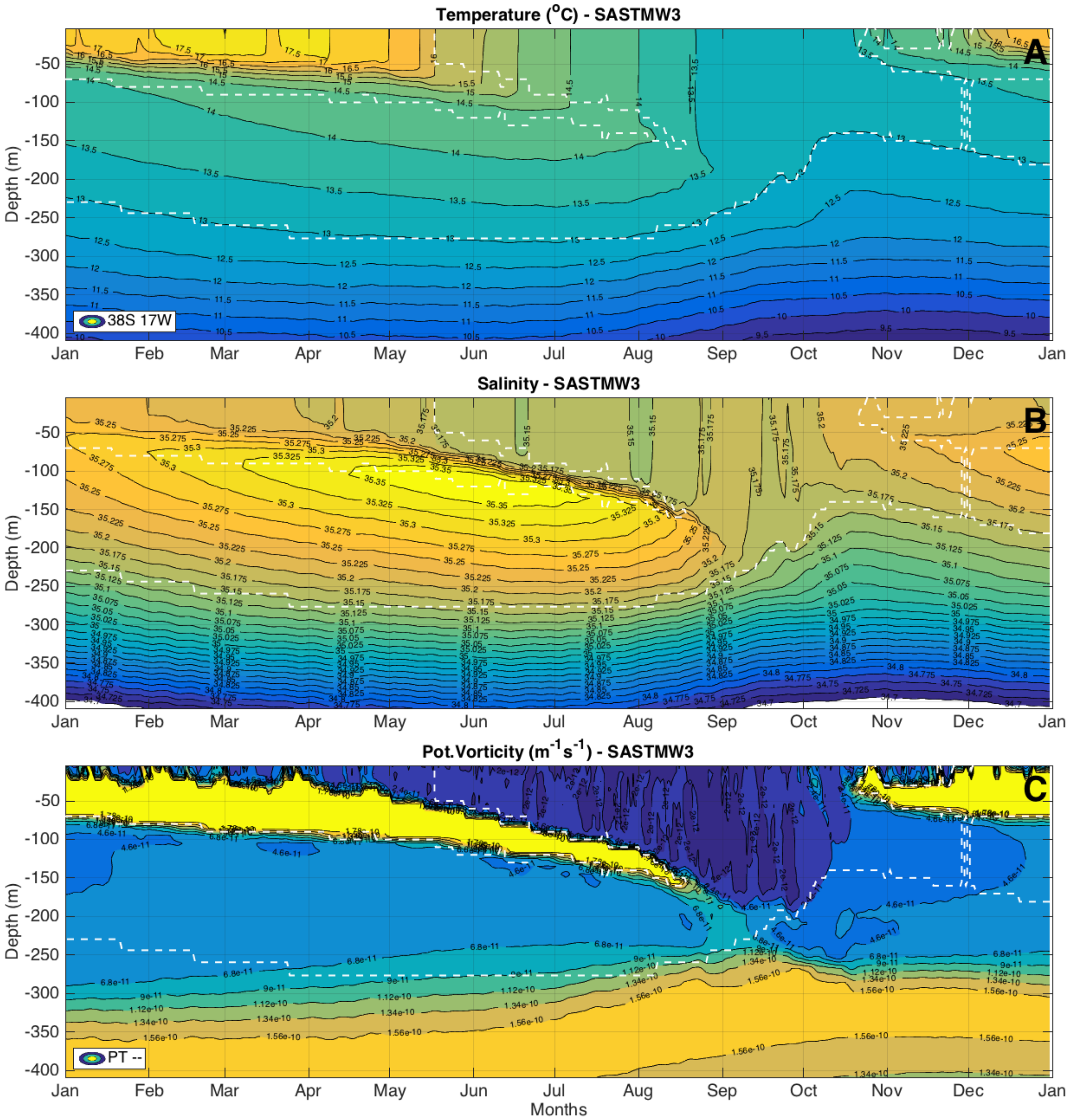

Figure S20. Temperature, shortwave radiation, salinity, precipitation, potential vorticity, and wind speed variation over one year at 38°S, 17°W in the CESM PT- experiment. The white contour represents the SASTMW 3 identified throughout the cycle. All the PV values greater than 1.5×10^{-10} m^{-1} s^{-1} were included in the maximum value contour.

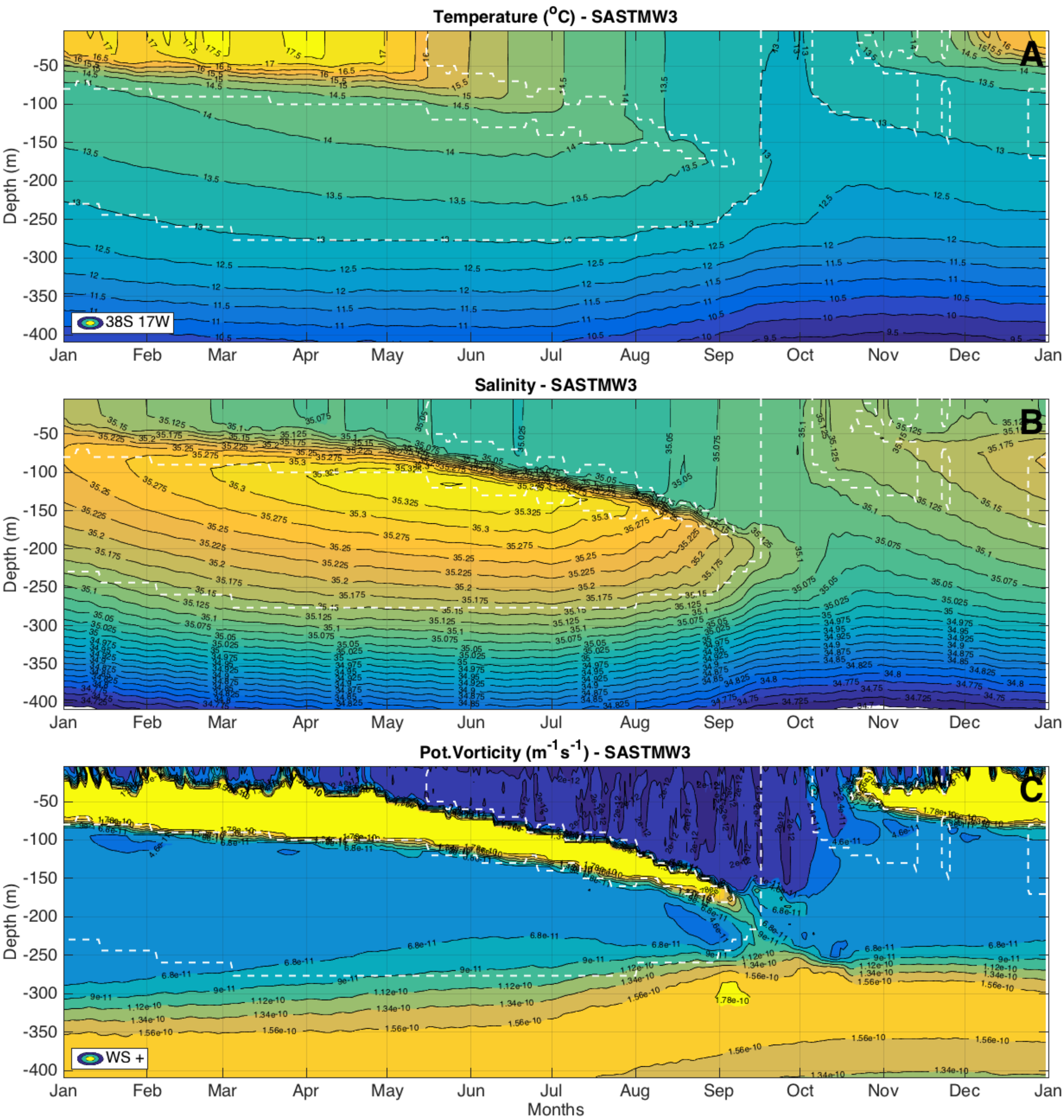

Figure S21. Temperature, shortwave radiation, salinity, precipitation, potential vorticity, and wind speed variation over one year at 38°S, 17°W in the CESM WS+ experiment. The white contour represents the SASTMW 3 identified throughout the cycle. All the PV values greater than 1.5×10^{-10} m^{-1} s^{-1} were included in the maximum value contour.

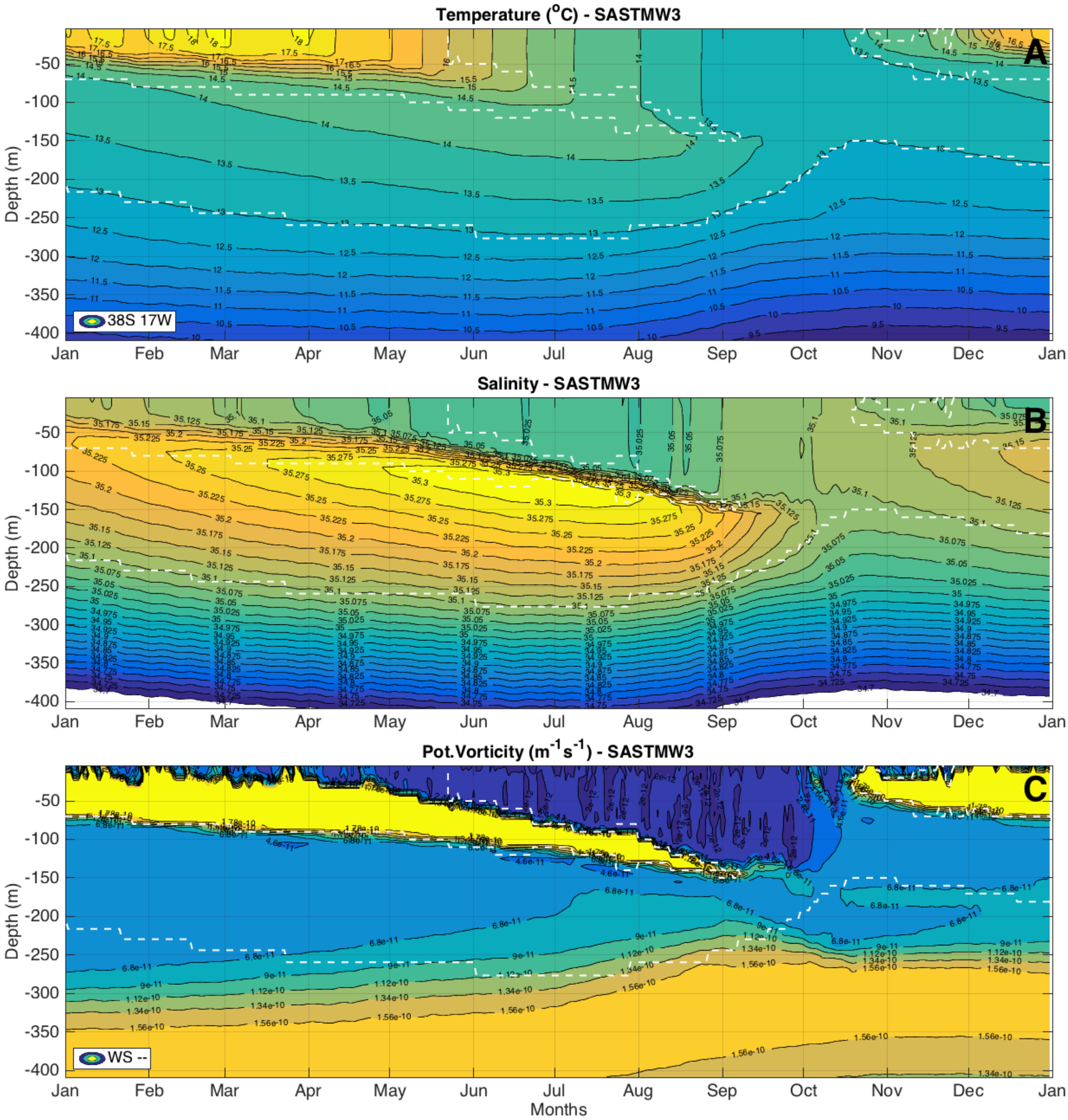

Figure S22. Temperature, shortwave radiation, salinity, precipitation, potential vorticity, and wind speed variation over one year at 38°S, 17°W in the CESM WS- experiment. The white contour represents the SASTMW 3 identified throughout the cycle. All the PV values greater than 1.5×10^{-10} m^{-1} s^{-1} were included in the maximum value contour.

Table S1. Values used for the sensitivity test of the selection of SASTMW related to the application of different criteria. Variables used as criteria: temperature (T); salinity (S); potential density (ρ); potential vorticity (PV) and vertical temperature gradient(dT/dz).

No.	Criteria Ref.	T (°C)	S	ρ (kg·m^{-3})	PV[a](m^{-1} s^{-1})	dT/dz (°C·m^{-1})
0	-	13 - 16	-	-	1.5	0.02
1	S	13 - 16	35 - 36	-	1.5	0.02
2	S and ρ	13 - 16	35 - 36	26.0 - 26.6	1.5	0.02
3	ρ	13 - 16	-	26.0 - 26.6	1.5	0.02
4	+dT/dz	13 - 16	-	-	1.5	0.1
5	-dT/dz	13 - 16	-	-	1.5	0.019
6	-dT/dz	13 - 16	-	-	1.5	0.015
7	-dT/dz	13 - 16	-	-	1.5	0.01
8	-dT/dz	13 - 16	-	-	1.5	0.005
9	+PV	13 - 16	-	-	5.0	0.02
10	-PV	13 - 16	-	-	1.4	0.02
11	-PV	13 - 16	-	-	1.0	0.02
12	-PV	13 - 16	-	-	0.5	0.02
13	-PV	13 - 16	-	-	0.2	0.02
14	T	12 - 18	-	-	1.5	0.02

[a] $\times 10^{-10}$.